J. Space Weather Space Clim. 2026, **16**, 14

https://doi.org/10.1051/swsc/2026013

JSWSC

Available online at:
www.swsc-journal.org

RESEARCH ARTICLE OPEN ACCESS

Assessing VB_z variations during CME propagation: a preparatory study for the HENON mission using EUHFORIA

Giuseppe Prete[1,*], Antonio Niemela[2,3], Stefaan Poedts[4,5], Gaetano Zimbardo[1,6], Stefano Cicalò[7], Maria F. Marcucci[8], Monica Laurenza[8], Mirko Stumpo[8], Simone Landi[9,10,11], Mattia Sangalli[9,10,11], Lorenzo Provinciali[12], Davide Monferrini[12], Davide Calcagno[12], Valerio Di Tana[12], Roger Walker[13], Francesco Pecora[14], Giuseppe Nisticò[1,6], Vincenzo Carbone[1,6,†], Federica Chiappetta[1], Antonella Greco[1,6], Fabio Lepreti[1,6], Francesco Malara[1,6], Silvia Perri[1,6], and Sergio Servidio[1,6]

[1]Department of Physics, University of Calabria, Ponte P. Bucci, Cubo 31C, Rende, Italy
[2]Heliospheric Physics Laboratory, Heliophysics Division, NASA Goddard Space Flight Center, Greenbelt, MD 20771, USA
[3]Goddard Planetary Heliophysics Institute, University of Maryland, Baltimore County, Baltimore, MD 21250, USA
[4]Centre for Mathematical Plasma Astrophysics, Dept. of Mathematics, KU Leuven, Celestijnenlaan 200B, 3001 Leuven, Belgium
[5]Institute of Physics, University of Maria Curie-Skłodowska, Pl. M. Curie-Skłodowska 5, 20-031 Lublin, Poland
[6]National Institute for Astrophysics, Scientific Directorate, Viale del Parco Mellini 84, I-00136 Roma, Italy
[7]Space Dynamics Services S.R.L., Navacchio di Cascina, Pisa, Italy
[8]Institute of Space Astrophysics and Planetology – INAF, Via del Fosso del Cavaliere 100, 00133 Roma, Italy
[9]Dipartimento di Fisica e Astronomia, Università degli Studi di Firenze, Via G. Sansone 1, 50019 Sesto Fiorentino, Italy
[10]INAF, Osservatorio Astrofisico di Arcetri, Largo E. Fermi 5, I-50125 Firenze, Italy
[11]INFN, Sezione di Firenze, Via G. Sansone 1, I-50019 Sesto Fiorentino (FI), Italy
[12]ARGOTEC S.R.L., San Mauro Torinese, Torino, Italy
[13]ESA-ESTEC, European Space Agency, Noordwijk, Netherlands
[14]Department of Physics and Astronomy, University of Delaware, Newark, DE 19716, USA

Received 21 October 2025 / Accepted 26 March 2026

Abstract – Coronal mass ejections (CMEs) are among the main drivers of space weather hazards. In this context, HENON is a new space mission designed to carry out observations in the solar wind upstream of the Earth, aiming to provide timely alerts for hazardous perturbations propagating towards the Earth. HENON will orbit Earth on a distant retrograde orbit, approximately 0.082 AU upstream of the Earth when it is on the Sun-Earth line. The measurements taken by HENON will allow us to determine plasma and magnetic field parameters with a lead time of several hours with respect to the Lagrangian point L1. We assess the VB_z parameter variations (the product of solar wind speed V and southward magnetic field B_z) along the HENON orbit. Given its role as a primary driver of geomagnetic activity, we analyze how these measurements change with respect to Earth's position to evaluate HENON's forecasting potential. We used the FRi3D CME model of the EUHFORIA simulation code to characterize the initial properties of the CME. FRi3D allows us to set the CME magnetic field as a magnetic flux rope. From the simulation results, we evaluated the VB_z parameter at nine virtual spacecraft positions along the planned HENON orbit. The heliocentric longitudes of the virtual spacecraft range from about $-6.9°$ to $6.9°$, while the geocentric longitudes vary from $-60°$ to $+60°$ in steps of $15°$. The initial direction of propagation of the CME central apex is either along the Sun-Earth line or at heliocentric longitudes of $\pm 30°$. We find that with the proposed orbital parameters, the values of the VB_z parameter along the HENON orbit is sufficiently similar to those measured in the vicinity of the Earth to be useful for space weather forecasts. At the same time, HENON permits to evaluate VB_z with a lead time of about 2−8 h, depending on the spacecraft position and the speed of the CME. The forecasting capabilities provided by HENON are expected to be foundational for the space weather community. This advancement has direct implications for enhancing the resilience of satellite communications and safeguarding critical infrastructure against space weather events.

Keywords: Coronal mass ejections / Geomagnetic storms / Geomagnetic indices / EUFHORIA simulations / HENON mission

*Corresponding author: giuseppe.prete@unical.it
† Deceased.

1 Introduction

The availability of early Space Weather (SW) warnings is of paramount importance for taking effective mitigation measures against space weather hazards (Echer et al., 2005; Gopalswamy, 2022). As is the case with forecasts of conventional weather, extended lead times and accurate predictions significantly improves our ability to reduce risks and minimize damage (Fry, 2012; MacAlester & Murtagh, 2014). Due to the diversity in the scales of the phenomena that influence and drive SW, this task is challenging.

Our current capabilities include (but are not limited to): remote sensing and imaging of the solar corona and photosphere in many different wavelengths, which target early identification of strong energy release sites (Brueckner et al., 1995; Kaiser et al., 2008; Lemen et al., 2012; Vourlidas et al., 2016; Antonucci et al., 2020); real-time in-situ monitors upstream of Earth (at the Lagrange point L1) (Acuña et al., 1995; Domingo et al., 1995; Smith et al., 1998) and close to Earth at geosynchronous orbit (Hill & Pizzo, 2003; Iyer et al., 2006; Loto'aniu et al., 2023; Stiefel et al., 2025); missions orbiting the Sun that provide a different perspective of these phenomena (Kaiser, 2005; Fox et al., 2016; Müller et al., 2020). Previous missions, such as STEREO (Webb et al., 2010; Ravishankar & Michałek, 2019), have transitioned the Lagrangian point L4 to monitor solar activity and space weather. Future missions are planned for both L4 and L5 (Gopalswamy et al., 2011; Rodriguez et al., 2020; Posner et al., 2021), including Vigil, which will focus on improving the SW forecasting (e.g., Eastwood et al., 2024). Furthermore, the recent PUNCH mission (DeForest et al., 2026), which consists of 4 imagers in a Sun-synchronous orbit around the Earth, will provide an unprecedented point of view on SW events.

In a comprehensive review, Vourlidas et al. (2019) suggested that an upstream monitor at 0.3 AU from Earth would be necessary to provide warnings of solar wind perturbations with approximately 24-h advance notice. However, Kepler's laws do not allow a spacecraft to stay stationary on the Sun-Earth line at 0.3 AU from the Earth on a free-fall (Keplerian two-body) orbit. As a first step in the direction upstream of the Earth, we can place a spacecraft at the collinear Lagrange point L1 of the Sun–Earth system, which lies at a much smaller distance, approximately 0.01 AU from Earth toward the Sun, than suggested by Vourlidas et al. (2019).

To go further upstream, in the planar circular restricted three-body problem, it is possible to take advantage of the specific type of orbits called Distant Retrograde Orbits (DROs), which were studied in detail by M. Hénon using Hill's approximation (Henon, 1969, 1970). In such a case, both the spacecraft and the Earth are orbiting around the Sun, and, because of the same semi-major axis (but different eccentricities), they have the same revolution period around the Sun. When viewed in the synodic reference frame (a rotating coordinate system commonly used for multi-body orbital degrees), the spacecraft trajectories display apparent retrograde motion relative to the planet, as shown in Figure 1.

The DRO approach is the theoretical framework that forms the basis of the HEliospheric pioNeer for sOlar and interplanetary threats defeNce (HENON) mission. The ESA-ASI HENON mission (Provinciali et al., 2024; Cicalò et al., 2025) aims to send a spacecraft on a DRO orbit to test the feasibility of the aforementioned approach. The HENON mission payload includes instruments to measure the solar wind plasma, magnetic field, and fluxes of energetic ions and electrons. The planned upstream distance of the spacecraft is about 0.082 AU, which allows a 2−8 h advance notice with respect to a spacecraft located in L1. For the HENON mission, the period of revolution around the Sun is 1 year (semi-major axis of 1 AU), and, depending on its eccentricity, the nominal orbit is chosen such that the spacecraft remains at a much larger distance from the Earth than the Lagrangian point L1 for an extended period. This orbital configuration offers a highly favorable conditions for real-time SW monitoring, while also ensuring stable relative orbital motion. Such a DRO allows a single spacecraft to dwell upstream of the Earth for only a limited time. Thus, a multispacecraft mission will be necessary to have continuous monitoring of solar wind conditions upstream of the Earth. A similar concept for an SW mission, the Diamond mission, (St. Cyr et al., 2000), envisioned a constellation of four spacecraft equally spaced along the same DRO at a minimum distance of 0.1 AU from Earth, but has never been realized. Possible exploitation of DROs for asteroid impact monitoring has also been proposed (Perozzi et al., 2017).

The possibility of sending space weather monitors upstream of L1, that is, of doing sub-L1 measurements, have been considered by several authors (e.g., Lugaz et al., 2024a, 2025; Palmerio, 2025). However, a crucial aspect to evaluate during the mission's planning phase is the correlation between observations acquired by the sub-L1 spacecraft and those obtained at Earth, given that the latter are more directly linked to SW disturbances. Indeed, it is well known that the interplanetary medium is characterized by complex physical phenomena, including shocks, turbulence, current sheets, and coherent structures (Bruno & Carbone, 2013; Matthaeus et al., 2015). These phenomena induce spatial and temporal variability in the properties of solar wind and energetic particles. For instance, Lugaz et al. (2018) found, by analyzing Wind and ACE data for a number of CMEs, that the magnetic field components at the two spacecraft are very well correlated when the longitudinal separation is less than 0.008 AU, which corresponds to the correlation length of the magnetic field at 1 AU (Ruiz et al., 2014; Cuesta et al., 2022), but the correlation decreases when the separation increases. Also, Scolini et al. (2024) analyzed the coherence of Alfvénic fluctuations within CMEs observed by ACE and Wind at a longitudinal separation of 0.009−0.013 AU, and found that the magnetic field profile seen by ACE and Wind is well correlated within the magnetic ejecta, but less so in the sheaths. However, we can argue that larger-scale structures, which are

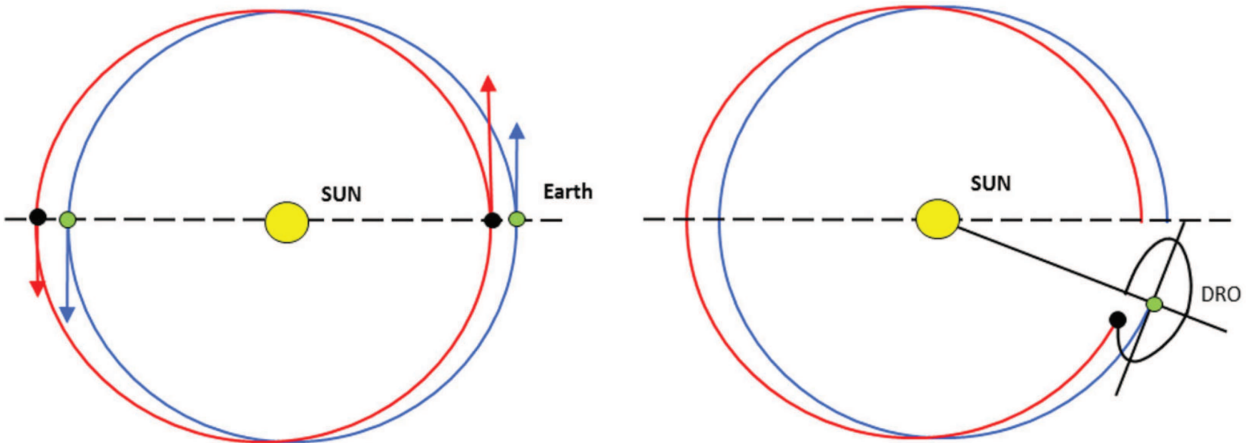

Figure 1. Dynamical configuration of DRO in the ecliptic plane, from Perozzi et al. (2017). In both panels, the heliocentric orbit of the Earth is depicted in blue, while the orbit of the satellite is shown in red. In the right panel, the spacecraft's trajectory with respect to the Earth's reference frame is shown in black.

more geoeffective, have larger scale coherence than Alfvenic fluctuations.

At the same time, CMEs evolve with radial distance, which also limits the radial separation between a sub-L1 monitor and the Earth. Using Solar Orbiter (Müller et al., 2020) as an upstream monitor at 0.5 AU, Laker et al. (2024) compared the observations for two CMEs, finding that in one case, the time profile of B_z was in good agreement between Solar Orbiter and Wind, despite of the radial distance and a longitudinal separation of about 10°. Regarding the second CME event, Laker et al. (2024) found that the magnetic structure was typical of two interacting flux ropes, but the agreement of the B_z time profile between spacecraft was poorer. Considering the strong geomagnetic storm of 10−12 May 2024, when the STEREO-A spacecraft was situated at 0.956 AU and 12.6° west of Earth, Weiler et al. (2025) find that the shock was observed 2.57 h earlier at STEREO-A than at L1, which is consistent with the shock speed of about 700 km s^{-1}. In addition, the B_z profiles showed good agreement, and the intensity of the geomagnetic storm was predicted well using STEREO-A data.

In another study, Lugaz et al. (2024b) analyzed the structure of magnetic ejecta in CMEs using STEREO-A and Wind data, finding that the typical angular size of magnetic ejecta is 20°–30° for most events, which is smaller than typically assumed. This implies that a sub-L1 monitor cannot stay too far away from the Sun-Earth line. In a recent comprehensive study on the properties required for a sub-L1 mission, Lugaz et al. (2025) suggest that a longitudinal separation from the sub-L1 monitor to the Sun-Earth line of $\lesssim$15° is needed, with a separation of less than 10° to be preferred to ensure that CMEs measured by the sub-L1 monitor also impact the geospace environment.

HENON orbit corresponds to 0.082 AU upstream of the Earth and to a maximum distance of ±0.164 AU along the y direction of the GSE system (Cicalò et al., 2025). In such a case, the maximum angular separation of HENON with the Sun-Earth line is ±9.3°. Furthermore, the prime region for space weather measurements, i.e., KR1, see Figure 2, is defined as ±60° in geocentric longitudes to stay upstream of the Earth: this corresponds to ±6.9° in heliocentric longitude. Therefore, HENON KR1 orbit is well within the angular separation recommended by Lugaz et al. (2025) for carrying out of useful measurements.

This paper investigates the relationship between observations from a virtual spacecraft situated on a DRO and those recorded at Earth. To achieve this, we employ a large-scale magnetohydrodynamic (MHD) simulation of the heliospheric structure, using the EUHFORIA code (EUropean Heliospheric FORecast Information Asset; Pomoell & Poedts, 2018). Additionally, we incorporate the orbital ephemerides of the operational DRO, which were numerically computed by SpaceDyS during the Phase A and B mission analysis studies for HENON (Provinciali et al., 2024; Cicalò et al., 2025). It should be noted that numerical simulations have a finite spatial resolution and that each model makes several assumptions, such as those regarding the coronal structure, the initial magnetic field, and the simulation domain. Global MHD simulations of the heliosphere are not yet able to resolve the small-scale structures of CMEs, and this should be taken into account when interpreting the simulation results; nevertheless, such simulations can provide very valuable information on the large scales.

We initialized EUHFORIA with a uniform background solar wind in which the CME is propagating. We compared the simulation results at HENON, located at various positions along the DRO, and on Earth. We performed several runs, varying the magnetic helicity of the initial magnetic flux rope that describes the CME magnetic field, as well as the direction of propagation of the CME relative to the Sun-Earth line, to study various scenarios for the interaction of CMEs with our planet. We use the FRi3D model (Maharana et al., 2022) of EUHFORIA to simulate the evolution of the CME. Among

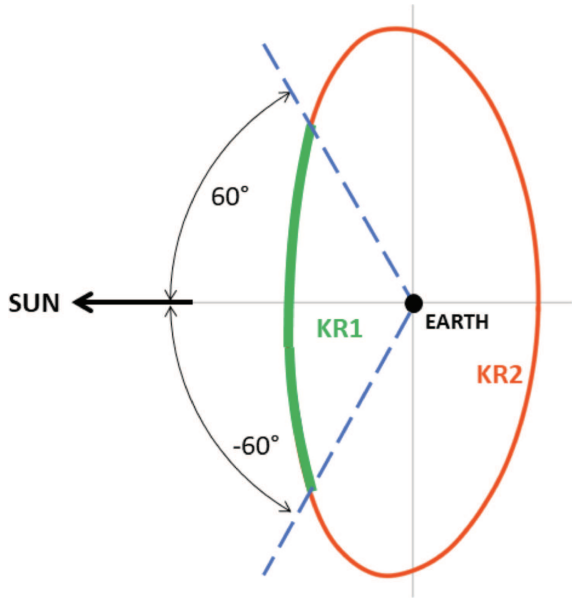

Figure 2. The HENON spacecraft orbits around the Earth. Key region 1 (KR1) and key region 2 (KR2) are also reported. The spacecraft geocentric longitudes are measured from the Earth-Sun line in the clockwise direction, in agreement with the retrograde motion of HENON. (Figure adapted from Cicalò et al., 2025).

the different quantities of interest for SW forecasts, we concentrate on VB_z, where V is the radial component of the solar wind velocity, and B_z is the vertical component of the interplanetary magnetic field (IMF) in the Geocentric Solar Magnetospheric (GSM) coordinate system. It is well-known that the parameter VB_z is an estimator for the reconnection electric field located at the nose of the Earth's magnetosphere. In this regard, VB_z demonstrates a notable correlation with the onset of geomagnetic storms (Gonzalez et al., 1989, 1994; Wang et al., 2003; Spencer et al., 2011). However, it is necessary to underline that VB_z remains only a proxy for the reconnection rate, considering that the electric field characteristic of the solar wind can differ from the field observed at the magnetopause (Borovsky & Birn, 2014).

Here, we focus on VB_z both because of its significance for geomagnetic storms and also because it is a typical parameter whose value can be evaluated at HENON and compared with measurements near Earth.

2 Geomagnetic storms, EUHFORIA model and numerical setup

2.1 Rationale

The product VB_z serves as a predictor for geomagnetic storm indices such as Dst, which is a measure of the intensity of the ring current around the Earth (Mayaud, 1980), and SYM-H, which quantifies the strength of a magnetic storm (Latiff et al., 2024). Numerous studies have established that intense geomagnetic storms (defined as Dst < -100 nT) are highly probable when the magnitude of the southward IMF component, $|B_z|$, exceeds 6−10 nT and the convection electric field, VB_z, is less than -5 mV/m for a duration exceeding 3 h (Gonzalez et al., 1989, 1994; Wang et al., 2003; Spencer et al., 2011; Verbanac et al., 2013). The threshold of -5 mV/m can be obtained, as an example, considering the solar wind plasma propagating at 500 km s^{-1} and carrying a southward magnetic field of 10 nT, i.e., $E_y = V_x B_z = 5 \times 10^5\,\mathrm{m\,s^{-1}} \times (-10^{-8})\,\mathrm{T} = -5 \times 10^{-3}\,\mathrm{V/m}$.

Consequently, a measurement period of at least 3 h in the solar wind is required following the arrival of an ICME at HENON before a geomagnetic storm alert can be reliably issued. For instance, to provide a 6-h advance alert, observations should begin 6 h before the southward turning of the magnetic field at Earth. Geoeffective ICME speeds near 1 AU typically range from 400−2000 km s^{-1}, with faster ICMEs generally correlating with more severe storms (Liu et al., 2014; Temmer & Nitta, 2015). Here, we assume an average geoeffective ICME speed of 700 km s^{-1} as a typical speed of the more common events. (Clearly, extreme events with large speeds are of the highest concern for space weather, and we reserve the study of larger speeds for the future.) A 6-h advance alert requires the sentinel spacecraft to be positioned at an upstream distance of approximately 15 120 000 km from Earth (∼0.1 AU). It is important to note that the lead time is reduced for CMEs faster than 700 km s^{-1}. Nonetheless, it is crucial to recognize that even relatively slow CMEs can exhibit significant geoeffectiveness, as highlighted by Gopalswamy et al. (2022).

To define efficient alert algorithms for the prediction of geomagnetic storms, we need to assess the difference in the observed VB_z at the Earth and along the HENON orbit using numerical simulations. We have been using two well-known global simulation models for the propagation of perturbations in the heliosphere, namely ENLIL (Odstrcil, 2003) and EUHFORIA (Pomoell & Poedts, 2018). Here, we present the results obtained with EUHFORIA. In the following simulations, we consider the evolution of a hypothetical CME, allowing us to select specific features and the positions of the observing spacecraft. Since the simulation epoch is arbitrary and not related to the inclination of the Earth's magnetic dipole and the Earth rotation, we will refer to the IMF component perpendicular to the ecliptic, namely B_z in the Geocentric Solar Ecliptic (GSE) coordinate system, and not to the actual southward component B_S in the Geocentric Solar Magnetospheric (GSM) system, which depends on time according to the Earth daily rotation and position along its heliocentric orbit. In any case, B_z is a good estimator of B_S (Wang et al., 2003).

2.2 EUHFORIA model

The EUHFORIA model, developed by Pomoell & Poedts (2018), is a space weather modeling tool that

computes the time evolution of the inner heliospheric plasma environment using a combination of empirical and physics-based modeling approaches. EUHFORIA consists of two major components: a coronal model and a heliospheric model. The data-driven coronal model uses synoptic magnetograms as input and provides solar wind plasma parameters at 0.1 AU from the Sun, utilising the empirical Wang-Sheeley-Arge model (Schatten et al., 1969; Altschuler & Newkirk, 1969; Arge et al., 2003). These are then used as boundary conditions to drive a 3D time-dependent MHD model of the inner heliosphere up to 2 AU. Different modeling approaches are available in EUHFORIA to simulate CME evolution, including the cone model (Xie et al., 2004), in which the CME has a spherical plasma bubble shape with a uniform density and no magnetic field structure; the spheromak model (Kataoka et al., 2009; Verbeke et al., 2019) that assumes a spherical shape for the CMEs with flux-rope structures; and the FRi3D (Flux Rope in 3 Dimensions, Isavnin, 2016; Maharana et al., 2022) model, which can reproduce the CMEs' shape and their deformations with a flux-rope internal structure. Previous runs (not shown) assumed the CME as a force-free spheromak, which gives rise, during CME propagation, to a magnetic flux rope structure (Chandrasekhar & Kendall, 1957; Shiota & Kataoka, 2016; Scolini et al., 2019; Verbeke et al., 2019).

The runs presented here were carried out with the latest FRi3D implementation in EUHFORIA (Maharana et al., 2022). In this novel version, the initial CME is described as a flux rope, according to the Graduated Cylindrical Shell (GCS; Thernisien et al., 2006; Thernisien, 2011) model. The GCS model is an empirical model widely used by the solar physics community for describing CMEs. The FRi3D model is an analytical model that provides the geometric shape of the CME and its deformations. It reproduces a cylindrical shell model filled with magnetic field lines. A series of parameters, such as the pancaking, i.e. the deformation of the frontal part of a flux rope during the expansion in the poloidal and toroidal direction, the flattening, which takes into account for the compression of the front part of the flux rope, and the rotational skew, namely the flux rope deformation due to the solar rotation, permit us to model the global shape of the CME accurately. The *Lundquist model* (Lundquist, 1950) is used to characterize the helical and twisted field lines in the force-free magnetic field distribution, with the aim of determining the magnetic field strength in a cylindrical geometry (for more details, see Maharana et al., 2022). A series of parameters has been set to shape the flux-rope inside the cylindrical shell: the angular half-width ($\varphi_{\rm hw}$), i.e., the maximum angular extension in the azimuthal direction, the angular half-height ($\varphi_{\rm hh}$), namely the maximum angular extension in the polar direction, the toroidal height (R_t) and the poloidal height (R_p), which indicates, respectively, the heliocentric distance to the apex of the CME axis and the radius of the cross-section at the apex of the CME. The total speed of the CME is given by the contribution of height growth due to linear propagation and the increase in the radial cross-section due to the pancaking effect $v_{\rm 3D} = \frac{\rm d}{{\rm d}t}(R_t + R_p) = v_{R_t} + v_{R_p}$. The magnetic field is characterized by five parameters: the tilt, i.e., the angular orientation of the CME axis measured from equatorial plane, the magnetic flux, namely the total magnetic flux of the CME, the twist, i.e., the number of turns in the magnetic field, the chirality that indicates the handedness of the flux-rope, and the polarity that gives the direction of the axial magnetic field of the flux-rope. Finally, the cylindrical shell is filled with a uniform-density plasma (see Table 1 in Maharana et al., 2022).

2.3 Simulation set-up

We conducted several runs, varying parameters such as the CME initial speed, the CME heliographic longitude, and the flux rope magnetic helicity sign. The solar wind conditions before the CME propagation have been set as uniform, with $n = 5.35\,{\rm cm}^{-3}$, $V = 472\,{\rm km\,s}^{-1}$ and $|B_r| = 2.10\,{\rm nT}$, to flatten the influence of coronal structures other than the CME. The use of EUHFORIA is advantageous compared to other heliospheric models because we can set the position of the observing spacecraft, and we can fix the CME's initial magnetic field properties. In addition, the high spatial resolution of EUHFORIA ($\Delta r = 0.004$ AU, $\Delta\theta = 2°$, $\Delta\phi = 2°$) enables the distinction, in the simulation results, between the formation of the CME-driven shock wave and the shocked sheath region preceding the magnetic cloud of the CME.

Furthermore, the orbital ephemerides of the HENON trajectory computed by SpaceDyS have been exploited to simulate the acquisition of measurements at nine distinct positions along the DRO within the key region 1 (KR1; see Fig. 2). Here, KR1 is defined as the region upstream of the Earth, which has a geocentric angular width of ±60° with respect to the Sun-Earth line. Looking from the Sun, the HENON longitudes in KR1 go from −6.9° to 6.9°. Typically, HENON will spend 90 days in KR1 and the rest of the year in key region 2 (KR2). For the present runs, the minimum upstream distance of HENON is 0.082 AU (Cicalò et al., 2025). To understand how the VB_z parameter would change along the DRO orbit and with respect to Earth, we have inserted nine virtual spacecraft, placed in KR1, spaced by 15° in terrestrial longitude, that cover the longitude range ±60° (as shown in Fig. 2) where the properties of the CME and the associated shock wave, obtained by the simulation, will be "monitored". The corresponding heliocentric longitudes are 0°, ±1.4°, ±2.9°, ±4.7°, and ±6.9°.

The simulation runs have been initialized with a CME speed of $750\,{\rm km\,s}^{-1}$, with a mass density of $10^{-17}\,{\rm kg\,cm}^{-3}$ and a temperature of 8×10^5 K. The time since CME insertion, ΔT, is 39 h. The parameters that are kept constant for all simulations are presented in Table 1. The parameters that were varied are presented in Table 2. In particular, the central latitude of the CME apex was set to zero, the central longitude of the CME apex was fixed either to zero or to ±30°, with a half-angle (the

Table 1. CME parameters used for all the simulations.

Parameter	Value
ΔT (h) since the insertion time of the CME	39
$V_{\rm CME}$ (km s^{-1})	750
R_t ($R_\odot$)	16.5
Half height (°)	15
Tilt angle (°)	0.5
Flattening	0.5
Pancaking	0.5
Twist	1
Polarity	+1
Flux (Wb)	10^{13}
Mass density (kg cm^{-3})	10^{-17}
Temperature (K)	8×10^5

Table 2. CME parameters used for the runs with the FRi3D model of EUHFORIA.

	RUN1	RUN2	RUN3	RUN4	RUN5	RUN6
Lat (°)	0	0	0	0	0	0
Lon (°)	0	0	30	30	−30	−30
Helicity	1	−1	1	−1	1	−1

half-width) between the CME legs of 30°, a tilt angle of 0.5° (that is, the CME croissant lies in the solar equatorial plane), and the magnetic helicity was set to +1 for left-handed chirality and −1 for right-handed chirality (Maharana et al., 2022). The FRi3D chirality is implemented, which uses an opposite convention with respect to the usual one. Clearly, many other physically relevant choices can be made for the simulation parameters, and we consider the present runs as a first study.

3 Simulation results

Figure 3 shows the simulation for RUN1. The upper panels show the density, rescaled by a factor $(r/1\,\mathrm{AU})^2$, and the lower panels show the radial velocity. For each quantity, the left panels show an equatorial cross-section, and the right panels show a meridional cross-section passing through the Earth, which is indicated by a yellow dot. The positions of the planets and the HENON spacecraft on the equatorial plane are also indicated as green squares. At approximately 0.082 AU, the CME-driven shock exhibits a clear density enhancement (∼20 cm^{-3}) relative to the ambient solar wind (∼4 cm^{-3}) (see panel a), along with a significantly higher speed of ∼700 km s^{-1} compared to the background solar wind velocity ∼500 km s^{-1} (see panel b).

Figure 4 shows the time profiles of several quantities measured by the virtual HENON spacecraft at 0.082 AU upstream of the Earth, and at the Earth. The panels, from top to bottom, display the magnetic field components and magnitude, plasma number density, velocity components and magnitude, temperature, and VB_z. At $\Delta T = 39$ h from the CME injection, each quantity exhibits a jump due to the CME-driven shock crossing. Just downstream of the shock, it is possible to recognize the sheath region characterized by a more disordered magnetic field, where the temperature increases abruptly. Past the sheath, the magnetic obstacle (the core of the helical flux tube inside the FRi3D) is located, where the magnetic field components B_y and B_z are observed to show the typical smooth rotation (Gosling, 1990), while the B_x component is almost zero. The VB_z time profile has a typical behavior for many geomagnetic storms (Wang et al., 2003), featuring small fluctuations around zero at the shock, followed by a gradual decrease of VB_z, down to values less than −5 mV/m, i.e., less than the threshold usually adopted for geomagnetic storm prediction for times longer than 3 h (Gonzalez & Tsurutani, 1987). The perturbation is first detected at HENON approximately 6 h before it is observed at Earth, consistent with the kinematic propagation of the ICMEs.

Figure 5 shows the simulated time series of all HENON virtual spacecraft and at the Earth for RUN1. In Figure 5, we use the following graphic conventions: the value of VB_z at the Earth is indicated by a solid green line, those at HENON, just in front of the Earth, by the solid purple line, those westward of the Earth-Sun line (i.e., with positive geocentric angles) by dotted lines in the shades of red, and those eastward of the Earth-Sun line (i.e., with negative geocentric angles) by dashed lines in shades of blue. A zoom on the negative VB_z peaks is shown in the inset of Figure 5 to better highlights the differences between the lines corresponding to the various virtual spacecraft.

As a general remark, we can see that the overall behavior of VB_z is similar at the Earth and at HENON, with little to no dependence on the longitudinal position of the virtual spacecraft within KR1. It can be seen that negative peak values are almost all larger at HENON, as compared to the Earth: this can be understood as the behavior of the transverse components of the interplanetary magnetic field, which scales with the heliocentric distance as $B_z \sim 1/r$, in agreement with the Parker spiral model, and as observed in a recent survey of the IMF (Maruca et al., 2023). With a positive helicity of the magnetic flux rope, the local magnetic field B_z is first negative and then positive. The negative values of VB_z reach −5 mV/m for more than three hours, indicating that a geomagnetic storm is expected. Thereafter, a prolonged period of positive VB_z is observed; this is due to the spacecraft being crossed by the magnetic axis of the CME magnetic flux rope, beyond which B_z turns from southward ($B_z < 0$) to northward ($B_z > 0$). The lead time is about 5.5 h when HENON is on the Earth-Sun line; one can see that this lead time decreases to about 3.5 h when HENON is at −60° (blue dashed line).

We consider that this decrease in lead time is due to the curved shape of the spacecraft trajectory, as shown in Figure 2, as well as the curved CME front (e.g., Shen et al., 2014). Interestingly, the decrease in lead time is not symmetric for the eastward and westward positions of HENON, as shown in Figure 5. This may be related to the deflection in the propagation of a CME when it

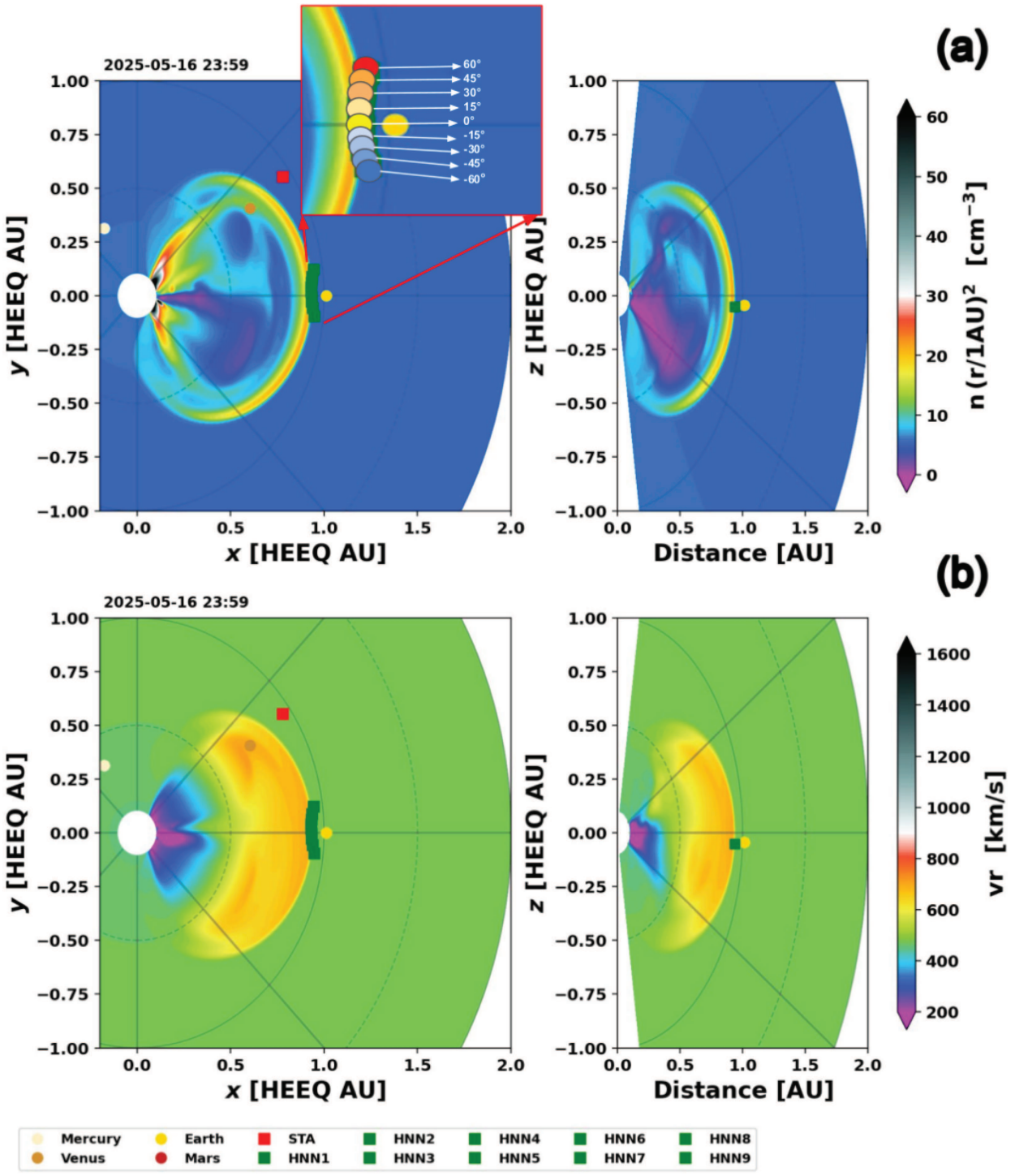

Figure 3. RUN1 simulation results at the time of arrival of the CME-driven shock at the HENON virtual spacecraft, indicated as HNN (see legend), positioned directly in front of the Earth, along the Sun-Earth line. Top row: detrended density in the equatorial plane (left) and in the meridional plane (right), with the colorbar on the right-hand side (panel a). Bottom row: radial velocity in the equatorial plane (left) and in the meridional plane (right), with the colorbar on the right-hand side (panel b). A yellow dot indicates the Earth's position, while green squares indicate the virtual spacecraft locations. In the inset we indicated the geocentric position of the virtual spacecraft in different colors.

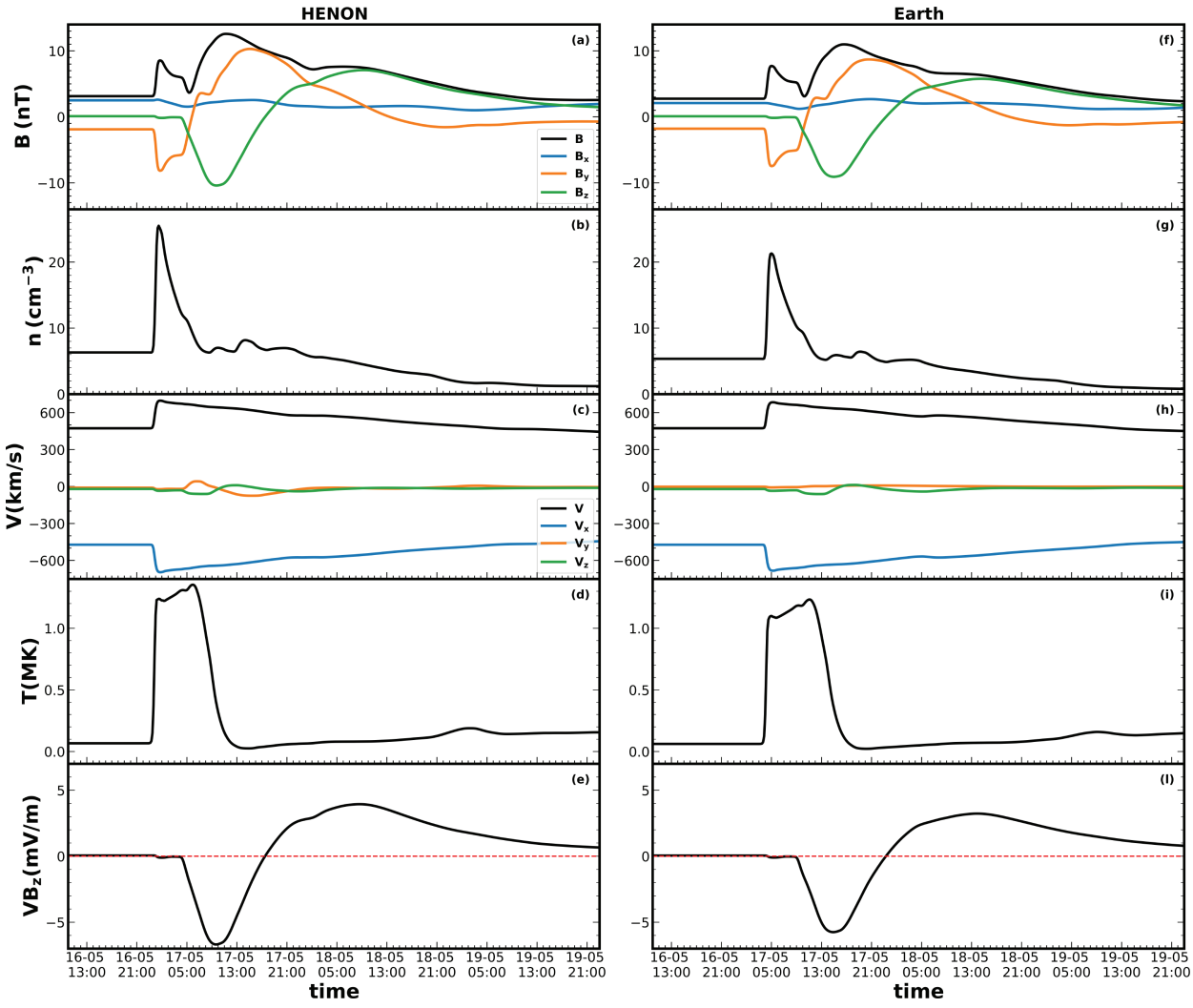

Figure 4. RUN1 simulation results. From top to bottom, the magnetic field components and strength, the plasma density, the bulk velocity components, the plasma temperature, and the VB_z parameter. Left panels: values at the HENON spacecraft upstream of the Earth on the Earth-Sun line; right panels: values at the Earth.

interacts with the spiral magnetic field of the solar wind. As shown by Wang et al. (2004), CMEs faster than the ambient solar wind are deflected eastward (looking from the Earth), while slower CMEs are deflected westward.

Figure 6 shows the same quantities as Figure 4 but for the case of RUN2. The overall behavior is similar to that of Figure 4. Due to this negative magnetic helicity, the magnetic field components inside the flux rope rotate oppositely, and therefore, the VB_z is first positive and then negative.

Figure 7 shows that in RUN2 VB_z is first positive and then negative, and the negative values are smaller than -3 mV/m for an extended period. The negative values reached by VB_z vary between -2 and -4 mV/m, and they are always greater than the -5 mV/m threshold for a geomagnetic storm. The overall behavior is in agreement with the results of positive magnetic helicity, that is, the behavior of VB_z at HENON is very similar to that at the Earth, and the perturbation is detected first at HENON with a lead time of about 5–6 h.

We also conducted several numerical simulations for the case where the CME heliographic central longitude does not align with the Sun-Earth line. Figure 8 (RUN3) shows the cross sections in the equatorial and meridional planes of the EUHFORIA simulation for density and radial component of the speed, when the CME is propagating towards +30°. In such a case, both Earth and HENON is crossed by the CME's eastern leg. The plasma and magnetic field parameters (not shown), for the case of positive helicity, show the shock and the plasma sheath. However, the increases in plasma quantities are slightly less abrupt and have a lower amplitude than in the case of propagation along the Sun-Earth line. This is expected since both the Earth and the virtual spacecraft are crossing the CME flank side, and almost *along* the flux rope leg (see left panel in Fig. 8).

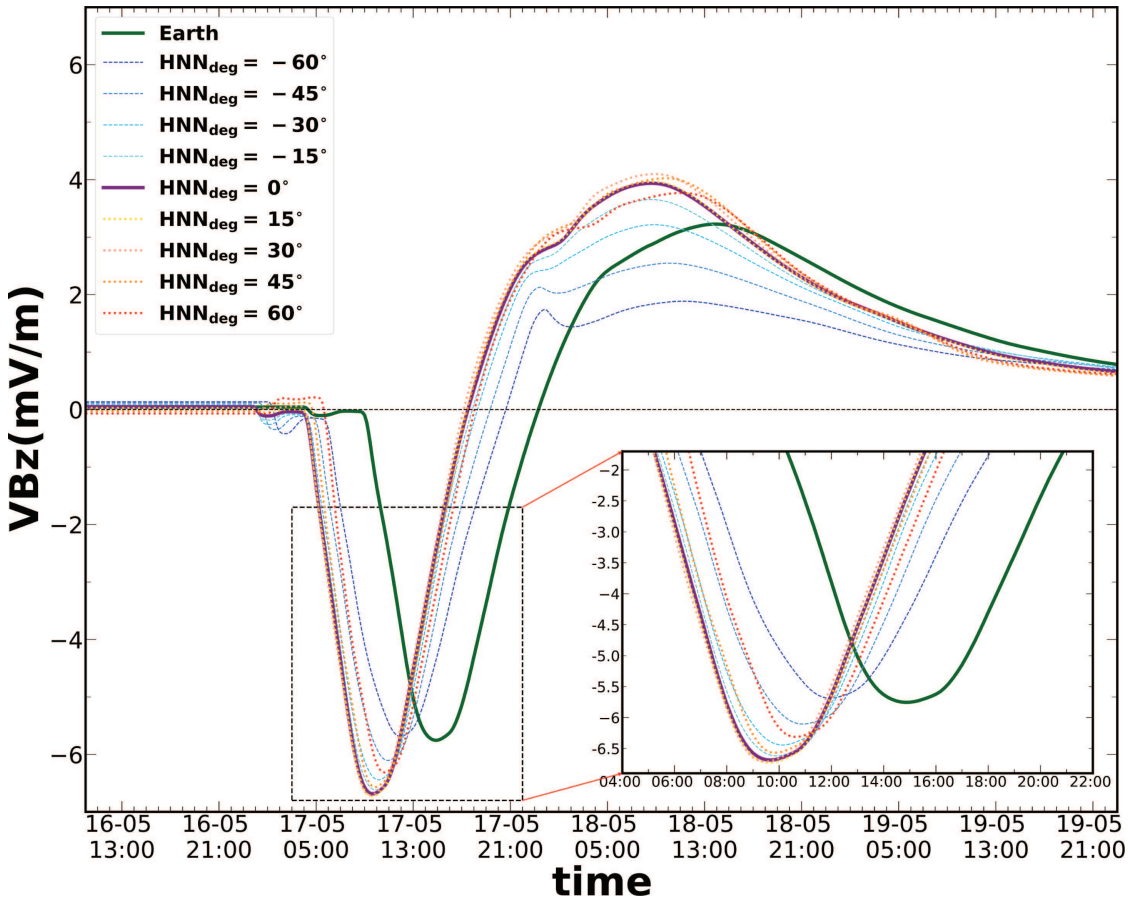

Figure 5. Variation of the VB_z parameter at the nine virtual spacecraft along KR1, plus at the Earth (solid green line), in the case of positive magnetic helicity. The geocentric longitudes of each spacecraft are indicated in the legend. VB_z is negative just after the shock crossing and then, because of the rotation of the magnetic field inside the flux rope, positive. In this case, VB_z becomes smaller than -5 mV/m for a period longer than 4 h, implying that a geomagnetic storm is possible. For later times, after the CME passage, VB_z tends towards small values, typical of unperturbed periods. The inset shows a magnified view of the VB_z profiles around the time of the negative peaks, as indicated by the dashed rectangle in the main panel.

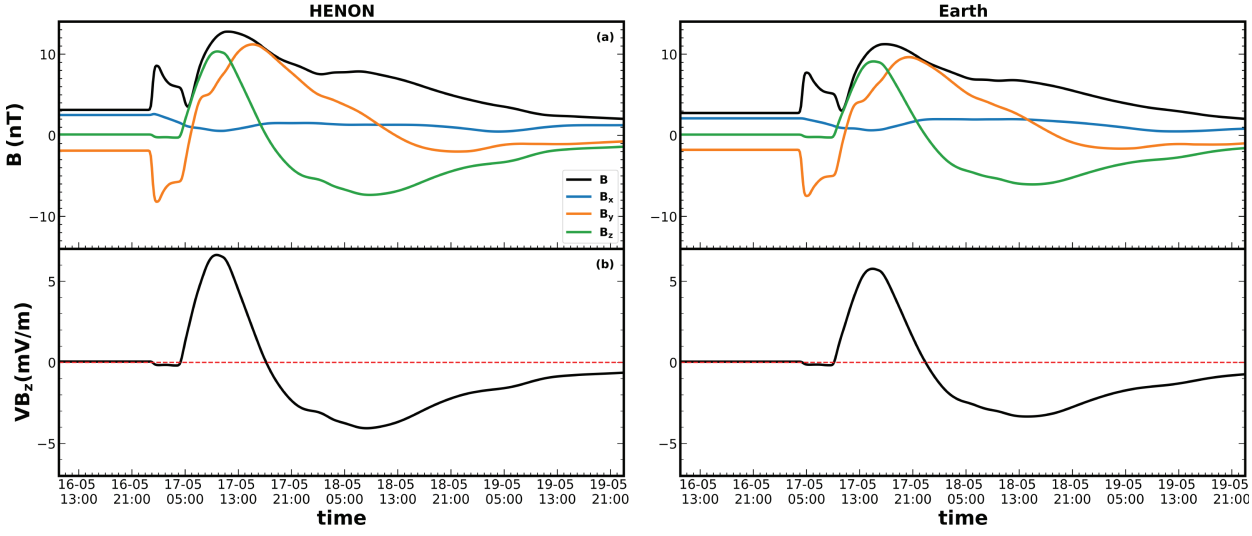

Figure 6. Same as Figure 4, but for the case of a magnetic flux rope with negative magnetic helicity (RUN2). The magnetic field rotates in the opposite direction, as compared to Figure 4.

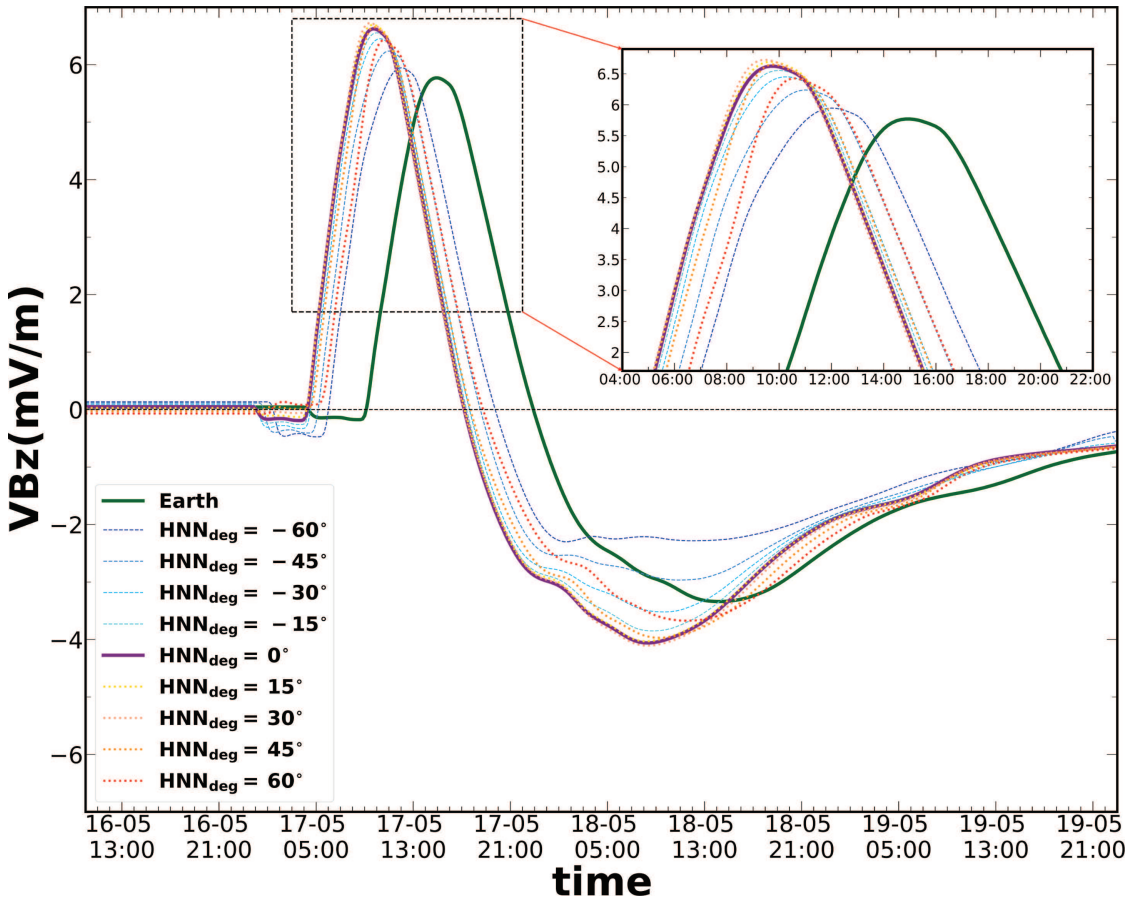

Figure 7. Same as Figure 5, but for negative magnetic helicity of the flux rope (RUN2). Now, VB_z is first positive and then negative; the negative values are smaller than −3 mV/m.

The VB_z parameter is shown in Figure 9a for positive magnetic helicity and in Figure 9b for negative magnetic helicity. From Figure 9a, we can see that the overall variations of VB_z are the same at HENON and at Earth. After the initial perturbation in VB_z (caused by the arrival of the shock and subsequent sheath), this quantity shows, a substantial decrease of VB_z within the FRi3D magnetic flux rope is obtained. However, now the lead time varies: while for spacecraft on positive geocentric longitudes, the VB_z variations are almost simultaneous with (or even earlier than) those at the HENON spacecraft just in front of the Earth (solid purple line), for a spacecraft located at negative geocentric longitudes, the variations of VB_z are progressively delayed with respect to the brown line, and the lead time with respect to the Earth is almost 2 h when HENON is at −60° of geocentric longitude. This can be understood by looking at the left panel in Figure 8, which shows that the CME curved front crosses the HENON spacecraft earlier when they are on positive geocentric longitudes (even earlier than the spacecraft on the Sun-Earth line), and later, when the spacecraft are on negative longitudes. We further notice that the peak values of VB_z change with the HENON longitude, the perturbation being larger when HENON is closer to the CME legs.

Figure 9b shows the corresponding results for RUN4. Now, the values of VB_z are primarily positive due to the change in the magnetic helicity. The results are similar to those of RUN3, with a simultaneous variation of VB_z for spacecraft located in front of the Earth and at positive geocentric longitudes, and a progressively delayed variation of VB_z for those at negative geocentric longitudes.

We can observe that, in the case of CME central longitude equal to 30° W, the B_z measured by the various spacecraft do not change sign as a function of time (not shown), it being either entirely positive or negative: we consider this to be due to the magnetic axis of the CME leg not crossing the spacecraft.

We have carried out numerical experiments also for the case of the CME pointing to the east (RUN5–6), i.e., for central apex longitude equal to 30° E: in this case, the CME western leg is overcoming HENON and the Earth, and the results are similar to those obtained for RUN3–4, but with the HENON spacecraft at negative geocentric longitudes seeing first the perturbation, as shown in Figure 10. The magnetic field and plasma parameters (not shown) at the HENON spacecraft on the Sun-Earth line and at the Earth are very similar, with peak values being larger at HENON.

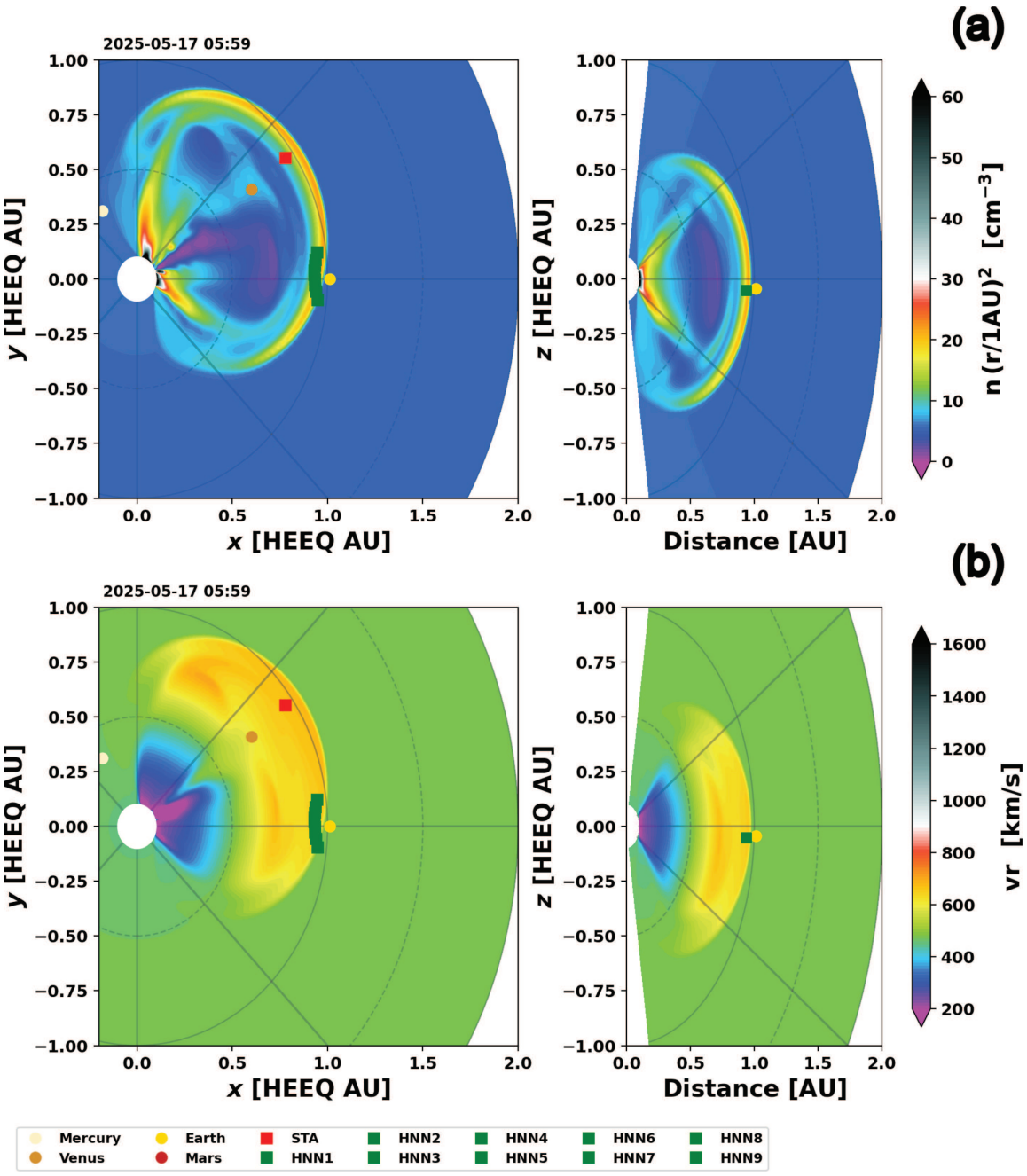

Figure 8. Simulation results RUN3, at the time when the CME is overcoming the HENON virtual spacecraft. Same format as Figure 3.

The VB_z parameter for RUN5 is shown in Figure 11a: in this case, too, the overall behavior is similar at HENON and at the Earth, but now the lead time is maximum (∼6 h) for the spacecraft on negative geocentric longitudes (shades of blue), while the lead time gradually decreases to about 1 h for spacecraft on positive geocentric longitudes (shades of red). In addition, the peak values of VB_z change with the position of the HENON spacecraft but remain larger than the values at the Earth, except for the spacecraft at 60° of geocentric longitude.

Figure 11b shows the corresponding results for RUN6, with the values of VB_z mainly being positive, due to the reversal in the sign of B_z registered at the virtual spacecraft after the passage of the sheath (not shown). As for the case of positive helicity (Fig. 11a), the variations of VB_z for spacecraft with negative geocentric longitudes are almost simultaneous with (or even earlier than) those at the spacecraft just in front of the Earth (solid purple line), while for the spacecraft on positive geocentric longitudes, the variations of VB_z are progressively delayed,

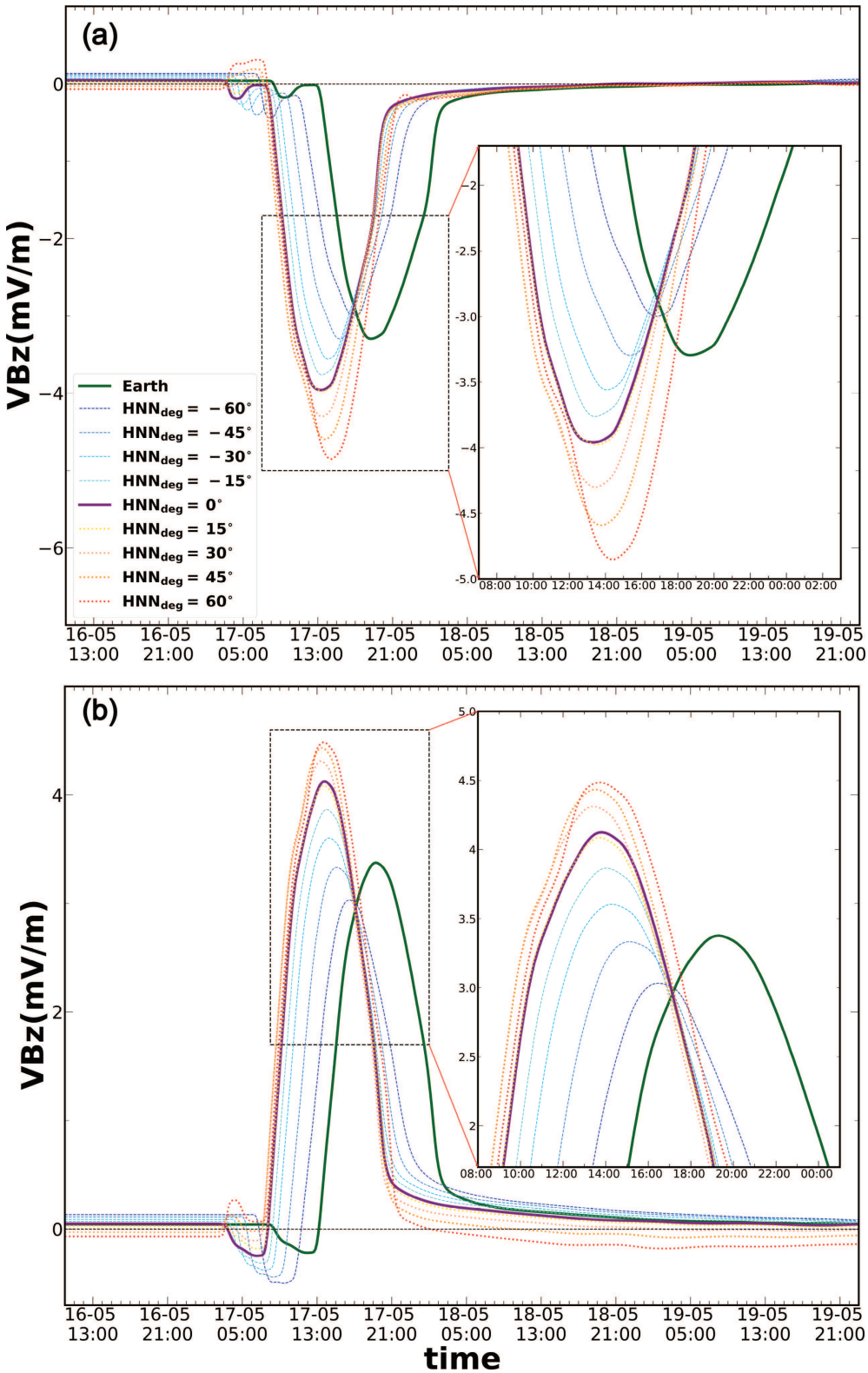

Figure 9. (a) Variation of the VB_z parameter at nine virtual spacecraft along KR1 and at Earth (thick green line), for the case of a CME propagating with central apex longitude equal to 30° W. Positive magnetic helicity is set in panel (a) (RUN3) and negative magnetic helicity is set in panel (b) (RUN4).

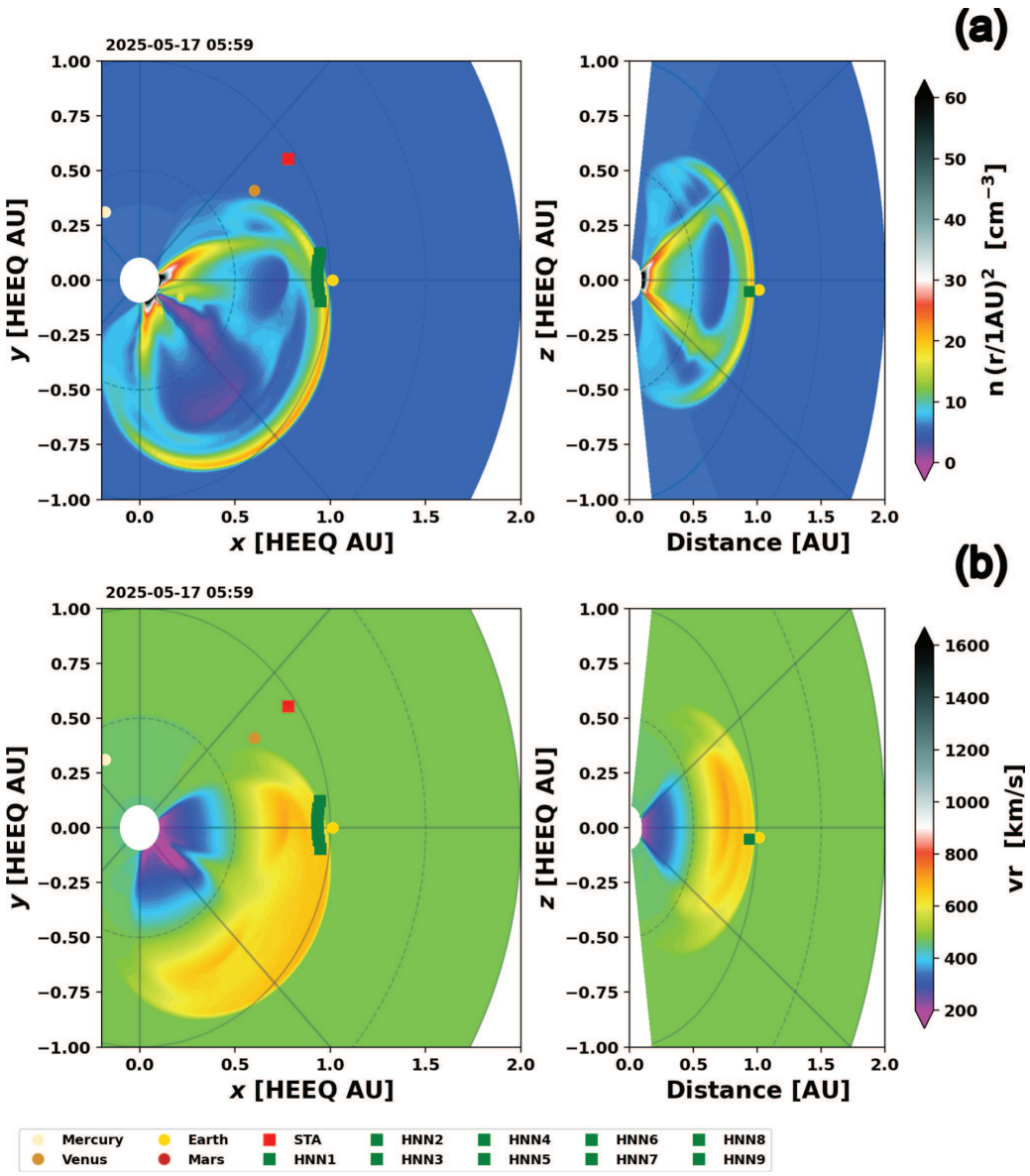

Figure 10. Simulation results for the flux rope central longitude corresponding to 30° E, at the time when the CME is overcoming the HENON virtual spacecraft. Same format as Figure 3.

with the lead time reduced to about 1 h for the spacecraft at +60° of geocentric longitude.

3.1 Predictive capabilities of the HENON mission

To better understand the results obtained for VB_z, we take the maximum of its absolute value as a function of the Alert time. We define the Alert time as the difference between the time corresponding to the maximum absolute value of VB_z at each position of the HENON virtual spacecraft and the corresponding time calculated at Earth

$$\text{Alert Time} = t_{\text{HENON}} - t_{\text{Earth}}.$$

This value is of fundamental importance for the early warning and mitigation of potentially hazardous geomagnetic disturbances.

In Figure 12, we show the maximum of the absolute value of VB_z for each virtual spacecraft and for each simulation. We indicate RUN1 and RUN2 with squares and circles; RUN3 and RUN4 with crosses and pentagons; and RUN5 and RUN6 with diamonds and triangles. For almost all configurations of CMEs and HENON positions within the KR1, the alert time is greater than 4 h. The largest values of $\max(|VB_z|)$ are reached when the CME is launched at 0° in both longitude and latitude (RUN1 and 2). The results from those runs are clustered in the top left side of the panel in Figure 12. In such a branch, we can notice that the best Alert Times are obtained when spacecraft are located within the longitude range

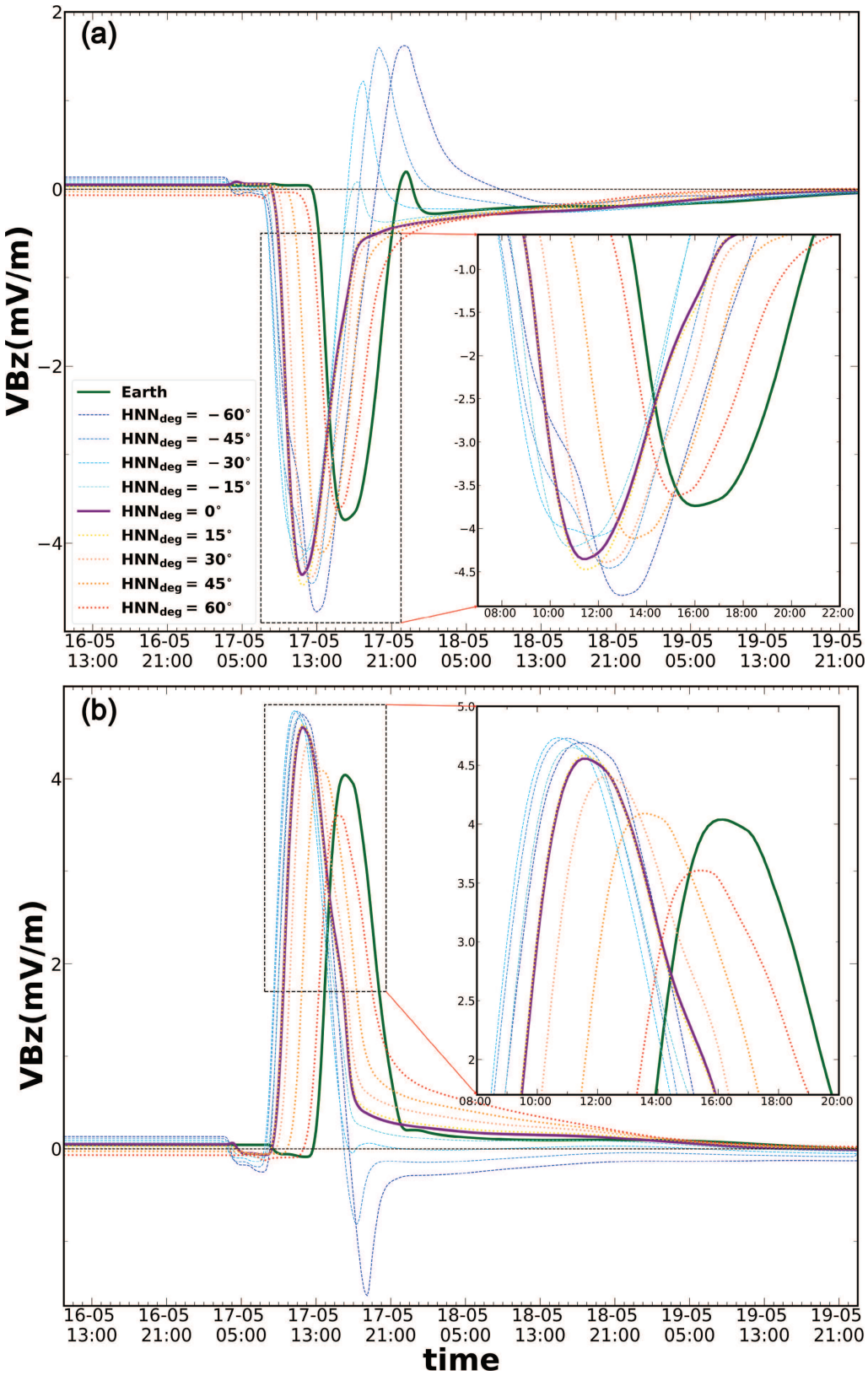

Figure 11. Variation of the VB_z parameter for the case of a CME propagating with central apex longitude equal to −30° and positive magnetic helicity. Same format as Figure 9.

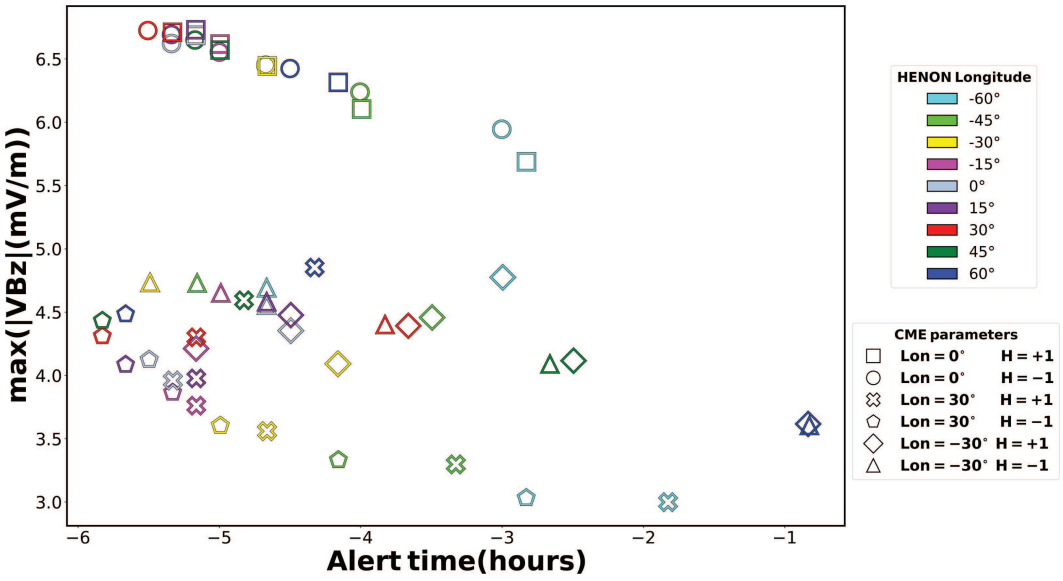

Figure 12. Alert Time at Earth for different CME events. All the CMEs have an initial speed of 750 km s^{-1}. The delay is measured as the difference between the time of the maximum of $|VB_z|$ recorded at the position of the HENON virtual spacecraft and the corresponding time measured at Earth. Squares and circles represent RUN1 and RUN2; crosses and pentagons represent RUN3 and RUN4; diamonds and triangles represent RUN5 and RUN6 (see legend CME parameters). The colour of each symbol indicates the spacecraft geocentric longitude (see legend).

between −45° and +60°, as the CME nose impacts these spacecraft head-on. This could be related to the interaction between the background solar wind and the CME, as the polarity of the background solar wind can influence the deformation and deflection of the CME. This may explain why, particularly away from the nose of the CME, the circles consistently shows a longer Alert Time than the squares.

Several differences arise when the CME is directed westward (RUN3 and 4) or eastward (RUN5 and 6) with respect to the Sun. It is evident that, in these cases, the values of max($|VB_z|$) are lower than for RUN1 and 2, as these virtual spacecraft have crossed the flank of the CME. Another surprising result concerns the Alert Time values, which in most cases are also greater than the previous ones. The best values are reached in RUN4 with an alert time of about 6 h.

Although the max($|VB_z|$) values oscillate between 3.5 and 5.0 mV/m, the corresponding Alert Times differ significantly. One would expect the CME to exhibit a symmetric behavior, giving rise to similar results in the Alert Time; however, a CME propagating westward arrives earlier than the one directed eastward. This can be related to the deflection of the CME in the interplanetary medium, as explained in Wang et al. (2004, 2014) and Zhuang et al. (2019). Indeed, in each run the CME speed exceeds that of the ambient solar wind, and the CME interacts with the Parker spiral field lines, which act like a "wall". This interaction produces a slight eastward deflection, even during radial propagation. Overall, the CME is guided in the direction of the spiral winding, i.e., the Parker spiral acts as a magnetic barrier, enhancing its motion in the eastward direction. This may explain why the Alert Times are longer in the case of westward-directed CMEs than in eastward-directed ones. In each simulation, virtual spacecraft are distributed over both positive and negative longitudes. However, when a fast CME is directed westward, it reaches the spacecraft at positive longitudes earlier than in the case of an eastward-directed CME reaching spacecraft at negative longitudes. In a symmetric scenario, one would expect that, for an eastward-directed CME, the spacecraft at negative longitudes would experience similar Alert Times. The fact that this is not observed suggests that the Parker spiral influences the CME propagation, effectively deflecting it in its direction of rotation, and causing an earlier arrival at the spacecraft located westward.

4 Conclusions

In this work, we investigated the potential of the HENON mission to serve as a forward observatory, providing timely SW alerts for CME events. HENON is a space mission designed to fly on a distant retrograde orbit around the Earth at an upstream distance of approximately 0.1 AU, allowing for advanced-time observations of SW perturbations that will impact Earth. To assess the relationship between delayed measurements at HENON and Earth, we focused on the VB_z parameter, which is considered a good predictor of the geomagnetic Dst index. An in-situ monitor like HENON is crucial to measure accurate magnetic field perturbations, in particular because the geoeffectiveness of a CME strongly depends on the sign of B_z. To explore the effects of an SW event along the whole KR1 of the orbit, we performed

6 different EUHFORIA simulations using the magnetized CME model FRi3D (Maharana et al., 2022). We positioned nine virtual spacecraft in front of the Earth within the KR1, covering geocentric longitudes from $-60°$ to $60°$, which correspond to heliocentric longitudes from $-6.9°$ to $6.9°$. For the present runs, the minimum upstream distance of HENON is 0.082 AU.

For the cases where the central apex longitude of the CME is zero (RUN1 and 2), that is, the CME is propagating along the Sun-Earth line, the simulation results show that the overall behaviour of VB_z is similar at HENON and on Earth, even when measurements are obtained at the limits (extremal longitudes) of KR1. This confirms the efficacy of the HENON mission for predictive purposes. With a positive helicity of the magnetic flux rope, the local magnetic field B_z is first negative and then positive. With the simulation parameters adopted, the negative values of VB_z reach -5 mV/m for more than three hours, indicating that a geomagnetic storm is likely to occur. Thereafter, a prolonged period of positive VB_z is obtained. According to the simulation results, a CME with positive helicity (RUN1) values appears to be more hazardous than one with negative helicity values (RUN2). As a consequence of the mission design, the variations of VB_z are detected at HENON with about 3.5 to 5.5 h of lead time for a CME propagating at more than 600 km s^{-1} along the radial direction. This represents a substantial improvement with respect to the observations carried out by spacecraft at L1. It is also found that the peak values of VB_z (positive and negative) are higher at HENON, compared to the Earth; this is understood as the transverse components of the interplanetary magnetic field scale with the heliocentric distance as $\sim 1/r$. Therefore, when using the threshold for the onset of geomagnetic storms, typically $VB_z < -5$ mV/m, one should take into account that the magnetic field transverse components at HENON are larger than those at Earth by a factor that depends on the heliocentric distance of HENON (r_{HENON}). In other words, to compare VB_z with the typical thresholds at Earth, the magnetic field should be multiplied by the factor $r_{\mathrm{HENON}}/r_{\mathrm{Earth}} < 1$. We point out, however, that other scalings for the magnetic field intensity in the magnetic flux rope of CMEs has been found (e.g., Davies et al., 2021), a possibility which should be taken into account. The radial dependence of the magnetic field magnitude has also been extensively investigated and reported to scale roughly as $r^{-1.6}$ in the inner heliosphere up to 1 AU (Maruca et al., 2022).

The lead time is approximately 5.5 h when HENON is on the Sun-Earth line; it can be seen that this lead time decreases to about 3.5 h when HENON is at $\pm 6.9°$ of heliocentric longitudes, corresponding to $\pm 60°$ of geocentric longitudes. We consider that this decrease in the advance time is due to the curved shape of the trajectory as well as to the curved CME front. These variations should also be taken into account when using the forthcoming HENON data for geomagnetic storm predictions. For the cases when the CME apex central longitude is not pointing directly to the Earth (RUN3 and 6), but is at $\pm 30°$ as in Figures 8–10, the shape of the perturbed VB_z is similar at HENON and at the Earth, but now the lead time varies: it is maximum, e.g., 6 h or more, when HENON is on the longitudes closest to the CME main direction of propagation, and up to the spacecraft on the Sun-Earth line; then the lead time gradually decreases, reaching a minimum of about 1−2 h for the case when HENON is on the edges of KR1, farthest from the CME trajectory. Therefore, in addition to knowing the HENON position on the orbit, it is crucial to understand the propagation direction of the CME.

Finally, we constructed a plot of the maximum value of $|VB_z|$ as a function of the Alert Time. The Alert Time is a relevant parameter derived in this work, as it provides an estimate of the signal delay between Earth and the position of the virtual spacecraft. Furthermore, we found that changing the CME's longitude affects the signal detected by the virtual spacecraft: contrary to expectations, minor differences emerge depending on the CME's direction. In fact, in the case of a westward-propagating CMEs, the virtual spacecraft located at positive longitudes exhibits longer Alert Times compared to the case of an eastward-directed CME. In a symmetric scenario, we would expect similar behavior for spacecraft located at negative longitudes, but this does not appear to occur. This asymmetry can be explained by the deflection in the CME propagation described by Wang et al. (2004, 2014) and Zhuang et al. (2019), who showed that a CME interacting with the interplanetary magnetic field will be deflected toward the east when it propagates faster than the background solar wind, and toward the west when it propagates slower than the background solar wind, due to the pileup of solar wind plasma ahead of or behind the CME. In the present simulations the CME speed is of the order of 700 km s^{-1} during the whole propagation outwards, while the background solar wind speed is below 500 km s^{-1}. Because the CME propagates faster than the ambient solar wind, an eastward deflection is observed. This is evident in Figure 3, which is slightly asymmetric and oriented eastward.

In this work, we present the simulation results for several cases. Clearly, different parameters like the flux rope tilt, the central apex longitude and latitude could be adopted, also keeping in mind that CMEs frequently are not centered on the heliographic equator (e.g., Zimbardo et al., 2023). When the CME is close to the heliographic equator and the central apex longitude is between $0°$ and $\pm 30°$, we can expect that the results for VB_z are intermediate between those shown here. Another issue to consider that the initial CME magnetic flux rope adopted in the simulations has a well-structured magnetic field configuration, which is reflected in the regularity and smoothness of the numerical results we have shown. However, real CMEs have a more complex and irregular magnetic structure, and even are deformed by their interaction with the background solar wind (Mayank et al., 2024), which could lead to larger differences in the VB_z profiles at the Earth and HENON, compared to those reported here. It should also be kept in mind that numerical simulations

have to make a number of simplifying assumptions. Therefore, the simulation results are important to develop the measurement scenario of the HENON project, but some degree of uncertainty regarding the above results should be taken into account. In addition, global heliospheric simulations cannot account for the small-scale interactions of CMEs with the turbulence of the interplanetary medium, which can lead to deformations and diffusion of structures on small scales (Sangalli et al., 2025).

We now note the following: a future development of the HENON space mission for continuous SW monitoring requires flying four spacecraft on the DRO, so that at least one spacecraft will always be in the KR1 orbit. This means that when one spacecraft is close to the limits of KR1 and on the opposite side of a CME propagating at, say, 30° W, there will be another spacecraft in KR2 (see Fig. 2) that will be in a favorable position to observe the passing CME. For instance, referring to Figure 9, a spacecraft in KR2 at geocentric longitudes between 60° and 90°, close to the CME, would observe a VB_z with a timing and intensity similar to those observed by a nearby spacecraft in KR1 at 45° or 60° of geocentric longitude. Such observations would have a lead time of ∼6 h, and would be very useful for geomagnetic storm predictions. Therefore, even a spacecraft in KR2 can play a significant role in SW, although the presence of small-scale structures, as discussed above, should be considered. Further simulations exploring different CME speeds, heliocentric longitudes and flux ropes tilts are planned and will be included in a dedicated database and described in a forthcoming paper.

These findings highlight that a robust space weather prediction infrastructure must incorporate, beside upstream in-situ monitors like HENON, continuous monitoring of solar eruptive activity (Vourlidas et al., 2019). This is essential for accurately determining the relative positions of HENON and any propagating CME, as our analysis demonstrates that the lead times, peak values of VB_z, and the feasibility of utilizing data from a spacecraft in KR2 depend critically on this relative positioning. We can conclude that the propagation direction of a CME is of fundamental importance in determining the potential severity of a geomagnetic storm. As shown by the simulations carried out, it is possible to issue a significant alert with a lead time of up to 6 h when the CME is directed frontally toward the Earth. An alert of a few hours is also possible, even when the CME is not precisely aligned with the Sun–Earth line. This represents an excellent result for geomagnetic storm forecasting, as it allows us to predict well in advance whether a specific event may pose a risk to space weather–related activities.

The increasing demand for reliable space weather forecasts necessitates a concerted effort from the heliophysics community to develop synergistic approaches that integrate both in-situ missions and remote observatories (Long et al., 2023). Current missions, such as Parker Solar Probe and Solar Orbiter, has significantly improved our knowledge of solar dynamics through in-situ observations near the Sun. Upcoming missions at L4 and L5, such as Vigil, will help to improve early detection of Earth-directed solar events. Polarized images from the new PUNCH mission can discern the direction of propagation of CMEs at their early onset, providing timely alerts for the whole network of remote and in-situ detectors such as HENON. Notably, the imminent and unprecedented observations provided by the PUNCH mission perfectly complement the in situ measurements from HENON, thereby enhancing our collective predictive capabilities.

Acknowledgments

The editor thanks Christian Möstl and Yuming Wang for their assistance in evaluating this paper.

Funding

This work is the outcome of the preparatory phases for the launch of the HENON mission by the Italian Space Agency (ASI) and was partially funded through the Argotec contracts, numbers ARG-IT-CON-P-HEN-220002 and ARG-IT-CON-P-HEN-250003. HENON is part of the ASI program Alcor and is being developed under the European Space Agency's General Support Technology Program (ESA-GSTP) through the support of the national delegations of Italy (ASI), the UK, Finland, and the Czech Republic. GZ, S. Perri, and GP acknowledge partial support by the Italian PRIN 2022, project 2022294WNB entitled "Heliospheric shocks and space weather: from multispacecraft observations to numerical modeling" (CUP H53D23000900006), funded by Next Generation EU, fondo del Piano Nazionale di Ripresa e Resilienza (PNRR) Missione 4 "Istruzione e Ricerca" – Componente C2 Investimento 1.1, Fondo per il Programma Nazionale di Ricerca e Progetti di Rilevante Interesse Nazionale (PRIN). S. Perri, GN, FC, and GZ acknowledge the project 'Data-based predictions of solar energetic particle arrival to the Earth: ensuring space data and technology integrity from hazardous solar activity events' (CUP H53D23011020001) 'Finanziato dall'Unione europea – Next Generation EU' PIANO NAZIONALE DI RIPRESA E RESILIENZA (PNRR) Missione 4 "Istruzione e Ricerca" – Componente C2 Investimento 1.1, 'Fondo per il Programma Nazionale di Ricerca e Progetti di Rilevante Interesse Nazionale (PRIN)' Settore PE09. FP acknowledges support by NASA/SWRI PUNCH subcontract N99054DS at the University of Delaware, and a Plan for NASA EPSCoR Research Infrastructure Development (RID) in Delaware (NASA award 80NSSC22M0039). SP is funded by the European Union. Views and opinions expressed are, however, those of the author(s) only and do not necessarily reflect those of the European Union or ERCEA. Neither the European Union nor the granting authority can be held responsible for them. This project (Open SESAME) has received funding under the Horizon Europe program (ERC-AdG agreement No 101141362). These results were also obtained in the framework of the projects C16/24/010 (C1 project Internal Funds KU Leuven), G0B5823N and G002523N (WEAVE) (FWO-Vlaanderen), and 4000145223 (SIDC Data Exploitation (SIDEX2), ESA Prodex).

Conflicts of interest

The authors declare no conflict of interest.

Data availability statement

The authors declare that no data are associated with this article.

References

Acuña MH, Ogilvie KW, Baker DN, Curtis SA, Fairfield DH, et al. 1995. The global geospace science program and its investigations. *Space Sci Rev* **71(1–4)**: 5–21. https://doi.org/10.1007/BF00751323.

Altschuler MD, Newkirk G. 1969. Magnetic fields and the structure of the solar corona. I: Methods of calculating coronal fields. *Sol Phys* **9(1)**: 131–149. https://doi.org/10.1007/BF00145734.

Antonucci E, Romoli M, Andretta V, Fineschi S, Heinzel P, et al. 2020. Metis: the Solar Orbiter visible light and ultraviolet coronal imager. *Astron Astrophys* **642**: A10. https://doi.org/10.1051/0004-6361/201935338.

Arge CN, Odstrcil D, Pizzo VJ, Mayer LR. 2003. Improved method for specifying solar wind speed near the Sun. In: *Solar Wind Ten. American Institute of Physics Conference Series*, Velli M, Bruno R, Malara F, Bucci B (Eds.), AIP, Vol. 679, pp. 190–193. https://doi.org/10.1063/1.1618574.

Borovsky JE, Birn J. 2014. The solar wind electric field does not control the dayside reconnection rate. *J Geophys Res (Space Phys)* **119(2)**: 751–760. https://doi.org/10.1002/2013JA019193.

Brueckner G, Howard R, Koomen M, Korendyke C, Michels D, et al. 1995. The large angle spectroscopic coronagraph (LASCO) visible light coronal imaging and spectroscopy. *Sol Phys* **162(1)**: 357–402. https://doi.org/10.1007/BF00733434.

Bruno R, Carbone V. 2013. The solar wind as a turbulence laboratory. *Liv Rev Sol Phys* **10(1)**: 2. https://doi.org/10.12942/lrsp-2013-2.

Chandrasekhar S, Kendall PC. 1957. On force-free magnetic fields. *Astrophys J* **126**: 457. https://doi.org/10.1086/146413.

Cicalò S, Alessi EM, Provinciali L, Amabili P, Saita G, et al. 2025. Mission analysis for the HENON CubeSat mission to a large Sun-Earth distant retrograde orbit. *Astrophys Space Sci* **370(8)**: 83. https://doi.org/10.1007/s10509-025-04473-0.

Cuesta ME, Chhiber R, Roy S, Goodwill J, Pecora F, et al. 2022. Isotropization and evolution of energy-containing eddies in solar wind turbulence: Parker solar probe, helios 1, ace, wind, and voyager 1. *Astrophys J Lett* **932(1)**: L11. https://doi.org/10.3847/2041-8213/ac73fd.

Davies EE, Forsyth RJ, Winslow RM, Möstl C, Lugaz N. 2021. A catalog of interplanetary coronal mass ejections observed by Juno between 1 and 5.4 au. *Astrophys J* **923(2)**: 136. https://doi.org/10.3847/1538-4357/ac2ccb.

DeForest CE, Gibson SE, Killough R, Waltham NR, Beasley MN, et al. 2026. Polarimeter to Unify the Corona and Heliosphere (PUNCH). *Sol Phys* **301(1)**: 16. https://doi.org/10.1007/s11207-026-02608-2.

Domingo V, Fleck B, Poland AI. 1995. The SOHO mission: an overview. *Sol Phys* **162(1–2)**: 1–37. https://doi.org/10.1007/BF00733425.

Eastwood JP, Brown P, Magnes W, Carr CM, Agu M, et al. 2024. The vigil magnetometer for operational Space Weather services from the Sun-Earth L5 point. *Space Weather* **22(6)**: e2024SW003867. https://doi.org/10.1029/2024SW003867.

Echer E, Gonzalez W, Guarnieri F, Dal Lago A, Vieira L. 2005. Introduction to space weather. *Adv Space Res* **35(5)**: 855–865. https://doi.org/10.1016/j.asr.2005.02.098.

Fox NJ, Velli MC, Bale SD, Decker R, Driesman A, et al. 2016. The solar probe plus mission: humanity's first visit to our star. *Space Sci Rev* **204(1–4)**: 7–48. https://doi.org/10.1007/s11214-015-0211-6.

Fry EK. 2012. The risks and impacts of space weather: policy recommendations and initiatives. *Space Policy* **28(3)**: 180–184. Highlight: Assuring the sustainability of space activities. https://www.sciencedirect.com/science/article/pii/S0265964612000616.

Gonzalez WD, Tsurutani, BT. 1987. Criteria of interplanetary parameters causing intense magnetic storms (Dst < -100 nT). *Planet Space Sci* **35(9)**: 1101–1109. https://www.sciencedirect.com/science/article/pii/0032063387900158.

Gonzalez WD, Tsurutani BT, Gonzalez ALC, Smith EJ, Tang F, et al. 1989. Solar wind-magnetosphere coupling during intense magnetic storms (1978–1979). *J Geophys Res* **94(A7)**: 8835–8851. https://doi.org/10.1029/JA094iA07p08835.

Gonzalez WD, Joselyn JA, Kamide Y, Kroehl HW, Rostoker G. 1994. What is a geomagnetic storm? *J Geophys Res* **99(A4)**: 5771–5792. https://doi.org/10.1029/93JA02867.

Gopalswamy N. 2022. The Sun and space weather. *Atmosphere* **13(11)**: 1781. https://doi.org/10.3390/atmos13111781.

Gopalswamy N, Davila JM, Cyr OS, Sittler EC, Auchère F, et al. 2011. Earth-Affecting Solar Causes Observatory (EASCO): A potential international living with a star mission from Sun–Earth L5. *J Atmos Solar-Terr Phys* **73(5–6)**: 658–663. https://doi.org/10.1016/j.jastp.2011.01.013.

Gopalswamy N, Yashiro S, Akiyama S, Xie H, Mäkelä P, et al. 2022. What is unusual about the third largest geomagnetic storm of solar cycle 24? *J Geophys Res (Space Phys)* **127(8)**: e30404. https://doi.org/10.1029/2022JA030404.

Gosling JT. 1990. Coronal mass ejections and magnetic flux ropes in interplanetary space, American Geophysical Union (AGU), pp. 343–364. ISBN 9781118663868. https://doi.org/10.1029/GM058p0343.

Henon M. 1969. Numerical exploration of the restricted problem, V. *Astron Astrophys* **1**: 223–238.

Henon M. 1970. Numerical exploration of the restricted problem. VI. Hill's case: Non-periodic orbits. *Astron Astrophys* **9**: 24–36.

Hill S, Pizzo VJ. 2003. Advanced solar imaging from the GOES R spacecraft. In: *Innovative Telescopes and Instrumentation for Solar Astrophysics*, Keil SL, Avakyan SV (Eds.), International Society for Optics and Photonics, SPIE, Vol. 4853, pp. 465–478. https://doi.org/10.1117/12.460385.

Isavnin A. 2016. FRiED: A novel three-dimensional model of coronal mass ejections. *Astrophys J* **833(2)**: 267. https://dx.doi.org/10.3847/1538-4357/833/2/267.

Iyer KN, Jadav RM, Jadeja AK, Manoharan PK, Sharma S, et al. 2006. Space Weather effects of coronal mass ejection. *J Astrophys Astron* **27(2–3)**: 219–226. https://doi.org/10.1007/BF02702524.

Kaiser ML. 2005. The STEREO mission: An overview. *Adv Space Res* **36(8)**: 1483–1488. https://doi.org/10.1016/j.asr.2004.12.066.

Kaiser ML, Kucera T, Davila J, St. Cyr O, Guhathakurta M, et al. 2008. The STEREO mission: An introduction. *Space Sci Rev* **136(1)**: 5–16. https://doi.org/10.1007/s11214-007-9277-0.

Kataoka R, Ebisuzaki T, Kusano K, Shiota D, Inoue S, et al. 2009. Three-dimensional MHD modeling of the solar wind structures associated with 13 December 2006 coronal mass ejection. *J Geophys Res (Space Phys)* **114(A10)**: A10102. https://doi.org/10.1029/2009JA014167.

Laker R, Horbury TS, O'Brien H, Fauchon-Jones EJ, Angelini V, et al. 2024. Using Solar Orbiter as an upstream solar wind monitor for real time Space Weather predictions. *Space Weather* **22(2)**: e2023SW003628. https://doi.org/10.1029/2023SW003628.

Latiff ZIA, Hairuddin MA, Zainuddin A, Ashar NDK, Jusoh MH. 2024. Analytical approach to SYM-H based geomagnetic storm classifications using statistical features extraction. *J Phys Conf Ser* **2915**: 012010. https://doi.org/10.1088/1742-6596/2915/1/012010.

Lemen JR, Title AM, Akin DJ, Boerner PF, Chou C, et al. 2012. The atmospheric imaging assembly (AIA) on the solar dynamics observatory (SDO). *Sol Phys* **275(1)**: 17–40. https://doi.org/10.1007/s11207-011-9776-81.

Liu YD, Luhmann JG, Kajdič P, Kilpua EKJ, Lugaz N, et al. 2014. Observations of an extreme storm in interplanetary space caused by successive coronal mass ejections. *Nat Commun* **5**: 3481. https://doi.org/10.1038/ncomms4481.

Long DM, Green LM, Pecora F, Brooks DH, Strecker H, et al. 2023. The eruption of a magnetic flux rope observed by Solar Orbiter and parker solar probe. *Astrophys J* **955(2)**: 152. https://dx.doi.org/10.3847/1538-4357/acefd5.

Loto'aniu PTM, Davis A, Jarvis A, Grotenhuis M, Rich FJ, et al. 2023. Initial on-orbit results from the GOES-18 spacecraft science magnetometer. *Space Sci Rev* **219(8)**: 84. https://doi.org/10.1007/s11214-023-01032-3.

Lugaz N, Farrugia CJ, Winslow RM, Al-Haddad N, Galvin AB, et al. 2018. On the spatial coherence of magnetic ejecta: Measurements of coronal mass ejections by multiple spacecraft longitudinally separated by 0.01 au. *Astrophys J Lett* **864(1)**: L7. https://doi.org/10.3847/2041-8213/aad9f4.

Lugaz N, Lee CO, Al-Haddad N, Lillis RJ, Jian LK, et al. 2024a. The need for near-Earth multi-spacecraft heliospheric measurements and an explorer mission to investigate interplanetary structures and transients in the near-Earth heliosphere. *Space Sci Rev* **220(7)**: 73. https://doi.org/10.1007/s11214-024-01108-8.

Lugaz N, Zhuang B, Scolini C, Al-Haddad N, Farrugia CJ, et al. 2024b. The width of magnetic ejecta measured near 1 au: Lessons from STEREO-A measurements in 2021–2022. *Astrophys J* **962(2)**: 193. https://doi.org/10.3847/1538-4357/ad17b9.

Lugaz N, Al-Haddad N, Zhuang B, Möstl C, Davies EE, et al. 2025. The need for a Sub-L1 space weather research mission: Current knowledge gaps on coronal mass ejections. *Space Weather* **23(2)**: 2024SW004189. https://doi.org/10.1029/2024SW004189.

Lundquist S. 1950. Magnetohydrostatic fields. *Ark Fys* **2**: 361–365. https://cir.nii.ac.jp/crid/1570009749193268480.

MacAlester MH, Murtagh W. 2014. Extreme space weather impact: An emergency management perspective. *Space Weather* **12(8)**: 530–537. https://doi.org/10.1002/2014SW001095.

Maharana A, Isavnin A, Scolini C, Wijsen N, Rodriguez L, et al. 2022. Implementation and validation of the FRi3D flux rope model in EUHFORIA. *Adv Space Res* **70(6)**: 1641–1662. https://doi.org/10.1016/j.asr.2022.05.056.

Maruca B, Qudsi RA, Alterman B, Walsh B, Korreck KE, et al. 2022. Radial trends in plasma parameters across the heliosphere. In: *AGU Fall Meeting Abstracts*, Vol. 2022, SH35D–1837.

Maruca BA, Qudsi RA, Alterman BL, Walsh BM, Korreck KE, et al. 2023. The trans-heliospheric survey. Radial trends in plasma parameters across the heliosphere. *Astron Astrophys* **675**: A196. https://doi.org/10.1051/0004-6361/202345951.

Matthaeus WH, Wan M, Servidio S, Greco A, Osman KT, et al. 2015. Intermittency, nonlinear dynamics and dissipation in the solar wind and astrophysical plasmas. *Philos Trans Roy Soc A: Math Phys Eng Sci* **373(2041)**: 20140154. https://royalsocietypublishing.org/doi/abs/10.1098/rsta.2014.0154.

Mayank P, Lotz S, Vaidya B, Mishra W, Chakrabarty D. 2024. Study of evolution and geo-effectiveness of coronal mass ejection–coronal mass ejection interactions using magnetohydrodynamic simulations with SWASTi framework. *Astrophys J* **976(1)**: 126. https://doi.org/10.3847/1538-4357/ad8084.

Mayaud PN. 1980. Derivation, meaning, and use of geomagnetic indices. *Geophys Monogr Ser* **22**: 607. https://doi.org/10.1029/GM022.

Müller D, St. Cyr OC, Zouganelis I, Gilbert HR, Marsden R, et al. 2020. The Solar Orbiter mission. Science overview. *Astron Astrophys* **642**: A1. https://doi.org/10.1051/0004-6361/202038467.

Odstrcil D. 2003. Modeling 3-D solar wind structure. *Adv Space Res* **32(4)**: 497–506. https://doi.org/10.1016/S0273-1177(03)00332-6.

Palmerio E. 2025. Monitoring the solar wind before it reaches L1. *Space Weather* **23(11)**: e2025SW004452. https://doi.org/10.1029/2025SW004452.

Perozzi E, Ceccaroni M, Valsecchi GB, Rossi A. 2017. Distant retrograde orbits and the asteroid hazard. *Eur Phys J Plus* **132(8)**: 367. https://doi.org/10.1140/epjp/i2017-11644-0.

Pomoell J, Poedts S. 2018. EUHFORIA: European heliospheric forecasting information asset. *J Space Weather Space Clim* **8**: A35. https://doi.org/10.1051/swsc/2018020.

Posner A, Arge CN, Staub J, StCyr OC, Folta D, et al. 2021. A multi-purpose heliophysics L4 mission. *Space Weather* **19(9)**: e2021SW002777. https://doi.org/10.1002/essoar.10506845.1.

Provinciali L, Calcagno D, Amabili P, Saita G, Riccobono D, et al. 2024. HENON – main challenges of a space weather alerts CubeSat mission. In: *2024 IEEE Aerospace Conference*, pp. 1–12. https://doi.org/10.1109/AERO58975.2024.10521299.

Ravishankar A, Michałek G. 2019. Estimation of arrival time of coronal mass ejections in the vicinity of the Earth using SOlar and Heliospheric Observatory and Solar TErrestrial RElations Observatory observations. *Sol Phys* **294(9)**: 125. https://doi.org/10.1007/s11207-019-1470-2.

Rodriguez L, Scolini C, Mierla M, Zhukov A, West M. 2020. Space weather monitor at the L5 point: A case

study of a CME observed with STEREO B. *Space Weather* **18(10)**: e2020SW002533. https://doi.org/10.1029/2020SW002533.

Ruiz ME, Dasso S, Matthaeus W, Weygand J. 2014. Characterization of the turbulent magnetic integral length in the solar wind: From 0.3 to 5 astronomical units. *Sol Phys* **289(10)**: 3917–3933.

Sangalli M, Verdini A, Landi S, Papini E. 2025. The effects of expansion and turbulence on the interplanetary evolution of a magnetic cloud. *Astron Astrophys* **699**: A258. https://doi.org/10.1051/0004-6361/202554559.

Schatten KH, Wilcox JM, Ness NF. 1969. A model of interplanetary and coronal magnetic fields. *Sol Phys* **6(3)**: 442–455. https://doi.org/10.1007/BF00146478.

Scolini C, Rodriguez L, Mierla M, Pomoell J, Poedts S. 2019. Observation-based modelling of magnetised coronal mass ejections with EUHFORIA. *Astron Astrophys* **626**: A122. https://doi.org/10.1051/0004-6361/201935053.

Scolini C, Lugaz N, Winslow RM, Farrugia CJ, Magyar N, et al. 2024. On the role of Alfvénic fluctuations as mediators of coherence within interplanetary coronal mass ejections: Investigation of multi-spacecraft measurements at 1 au. *Astrophys J* **961(1)**: 135. https://doi.org/10.3847/1538-4357/ad0ed1.

Shen C, Wang Y, Pan Z, Miao B, Ye P, et al. 2014. Full-halo coronal mass ejections: Arrival at the Earth. *J Geophys Res (Space Phys)* **119(7)**: 5107–5116. https://doi.org/10.1002/2014JA020001.

Shiota D, Kataoka R. 2016. Magnetohydrodynamic simulation of interplanetary propagation of multiple coronal mass ejections with internal magnetic flux rope (SUSANOO-CME). *Space Weather* **14(2)**: 56–75. https://agupubs.onlinelibrary.wiley.com/doi/abs/10.1002/2015SW001308.

Smith CW, L'Heureux J, Ness NF, Acuña MH, Burlaga LF, et al. 1998. The ACE magnetic fields experiment. *Space Sci Rev* **86**: 613–632. https://doi.org/10.1023/A:1005092216668.

Spencer E, Kasturi P, Patra S, Horton W, Mays ML. 2011. Influence of solar wind-magnetosphere coupling functions on the Dst index. *J Geophys Res (Space Phys)* **116(A12)**: A12235. https://doi.org/10.1029/2011JA016780.

St. Cyr OC, Mesarch MA, Maldonado HM, Folta DC, Harper AD, et al. 2000. Space Weather Diamond: A four spacecraft monitoring system. *J Atmos Solar-Terr Phys* **62(14)**: 1251–1255. https://doi.org/10.1016/S1364-6826(00)00069-9.

Stiefel MZ, Kuhar M, Limousin O, Dickson ECM, Volpara A, et al. 2025. Using the STIX background detector as a proxy for GOES. *Astron Astrophys* **694**: A138. https://doi.org/10.1051/0004-6361/202452574.

Temmer M, Nitta NV. 2015. Interplanetary propagation behavior of the fast coronal mass ejection on 23 July 2012. *Sol Phys* **290(3)**: 919–932. https://doi.org/10.1007/s11207-014-0642-3.

Thernisien A. 2011. Implementation of the graduated cylindrical shell model for the three-dimensional reconstruction of coronal mass ejections. *Astrophys J Suppl* **194(2)**: 33. https://doi.org/10.1088/0067-0049/194/2/33.

Thernisien AFR, Howard RA, Vourlidas A. 2006. Modeling of flux rope coronal mass ejections. *Astrophys J* **652(1)**: 763–773. https://doi.org/10.1086/508254.

Verbanac G, Živković S, Vršnak B, Bandić M, Hojsak T. 2013. Comparison of geoeffectiveness of coronal mass ejections and corotating interaction regions. *Astron Astrophys* **558**: A85. https://doi.org/10.1051/0004-6361/201220417.

Verbeke C, Pomoell J, Poedts S. 2019. The evolution of coronal mass ejections in the inner heliosphere: Implementing the spheromak model with EUHFORIA. *Astron Astrophys* **627**: A111. https://doi.org/10.1051/0004-6361/201834702.

Vourlidas A, Howard RA, Plunkett SP, Korendyke CM, Thernisien AF, et al. 2016. The wide-field imager for solar probe plus (WISPR). *Space Sci Rev* **204(1)**: 83–130. https://doi.org/10.1007/s11214-014-0114-y.

Vourlidas A, Patsourakos S, Savani NP. 2019. Predicting the geoeffective properties of coronal mass ejections: Current status, open issues and path forward. *Philos Trans Roy Soc London Ser A* **377(2148)**: 20180096. https://doi.org/10.1098/rsta.2018.0096.

Wang Y, Shen CL, Wang S, Ye PZ. 2003. An empirical formula relating the geomagnetic storm's intensity to the interplanetary parameters: $-VB_z$ and Δt. *Geophys Res Lett* **30(20)**: 2039. https://doi.org/10.1029/2003GL017901.

Wang Y, Shen C, Wang S, Ye P. 2004. Deflection of coronal mass ejection in the interplanetary medium. *Sol Phys* **222(2)**: 329–343. https://doi.org/10.1023/B:SOLA.0000043576.21942.aa.

Wang Y, Wang B, Shen C, Shen F, Lugaz N. 2014. Deflected propagation of a coronal mass ejection from the corona to interplanetary space. *J Geophys Res (Space Phys)* **119(7)**: 5117–5132. https://doi.org/10.1002/2013JA019537.

Webb D, Biesecker D, Gopalswamy N, Cyr OS, Davila J, et al. 2010. Using STEREO-B as an L5 space weather pathfinder mission. *Space Res Today* **178**: 10–16.

Weiler E, Möstl C, Davies EE, Veronig AM, Amerstorfer UV, et al. 2025. First observations of a geomagnetic superstorm with a sub-L1 monitor. *Space Weather* **23(3)**: 2024SW004260. https://doi.org/10.1029/2024SW004260.

Xie H, Ofman L, Lawrence G. 2004. Cone model for halo CMEs: Application to space weather forecasting. *J Geophys Res (Space Phys)* **109(A3)**: A03109. https://doi.org/10.1029/2003JA010226.

Zhuang B, Wang Y, Hu Y, Shen C, Liu R, et al. 2019. Numerical simulations on the deflection of coronal mass ejections in the interplanetary space. *Astrophys J* **876(1)**: 73. https://doi.org/10.3847/1538-4357/ab139e.

Zimbardo G, Ying B, Nisticò G, Feng L, Rodríguez-García L, et al. 2023. A high-latitude coronal mass ejection observed by a constellation of coronagraphs: Solar Orbiter/Metis, STEREO-A/COR2, and SOHO/LASCO. *Astron Astrophys* **676**: A48. https://doi.org/10.1051/0004-6361/202346011.

Cite this article as: Prete G, Niemela A, Poedts S, Zimbardo G, Cicalò S, et al. 2026. Assessing VB_z variations during CME propagation: a preparatory study for the HENON mission using EUHFORIA. *J. Space Weather Space Clim.* **16**, 14. https://doi.org/10.1051/swsc/2026013.